New experimental evidence for pervasive dynamics in proteins.

Erik R.P. Zuiderweg[1,2,*] and David A. Case[3]

1) *Radboud University, Institute for Molecules and Materials, 6525 XZ Nijmegen, The Netherlands*

2) *University of Michigan Medical School, Department of Biological Chemistry, Ann Arbor, MI 41109, USA*

3) *Rutgers University, Department of Chemistry & Chemical Biology*
Piscataway, NJ 08854, USA

* Correspondence to zuiderwe@umich.edu

Abstract

There is ample computational, but only sparse experimental data suggesting that pico-ns motions with 1 Å amplitude are pervasive in proteins in solution. Such motions, if present in reality, must deeply affect protein function and protein entropy. Several NMR relaxation experiments have provided insights into motions of proteins in solution, but they primarily report on azimuthal angle variations of vectors of covalently-linked atoms. As such, these measurements are not sensitive to distance fluctuations, and cannot but under-represent the dynamical properties of proteins. Here we analyze a novel NMR relaxation experiment to measure amide proton transverse relaxation rates in uniformly ^{15}N labeled proteins, and present results for protein domain GB1 at 283 and 303K. These relaxation rates depend on fluctuations of dipolar interactions between ^{1}HN and many nearby protons on both the backbone and sidechains. Importantly, they also report on fluctuations in the distances between these protons.
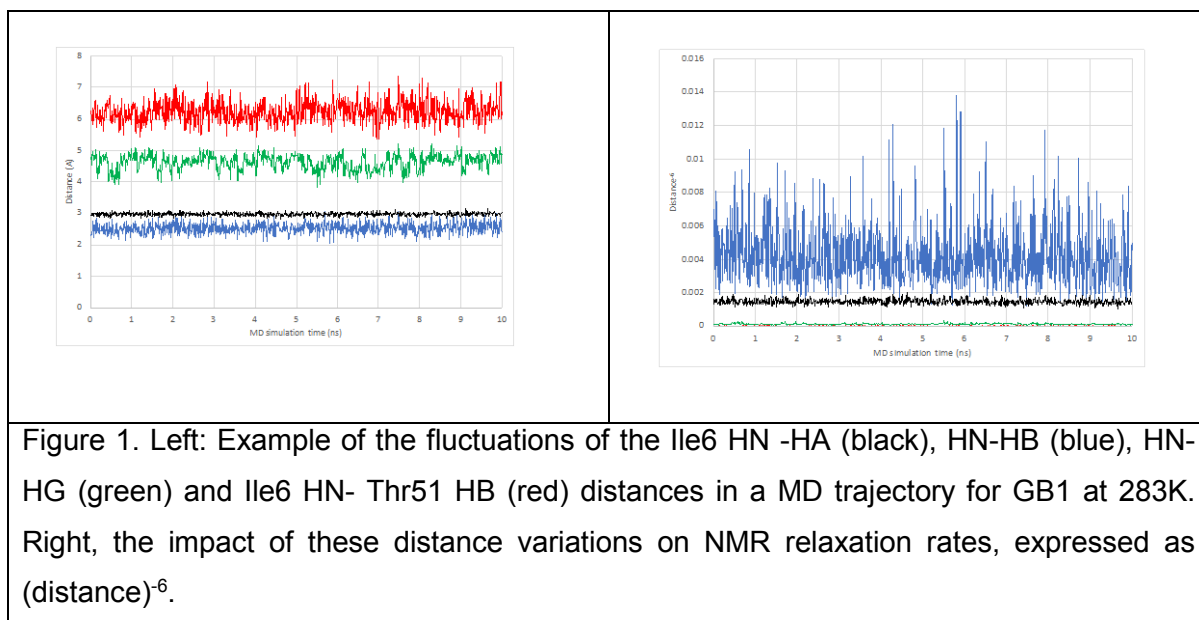
We obtained a large mismatch between rates computed from the crystal structure of GB1 and the experimental rates. But when the relaxation rates were calculated from a 200 ns molecular dynamics trajectory using a novel program suite, we obtained a substantial improvement in the correspondence of experimental and theoretical rates.

As such, this work provides novel experimental evidence of widespread motions in proteins. Since the improvements are substantial, but not sufficient, this approach may also present a new benchmark to help improve the theoretical forcefields underlying the molecular dynamics calculations.

1. Introduction.

Computational protein molecular dynamics programs (MD) such as AMBER (1) GROMOS (2), GROMACS (3) or CHARMM (4) use non-quantum mechanical forcefields that are calibrated on physico-chemical parameters of ensembles of small molecules. Computations using such force fields predict that pico-ns motion with at least 0.1 nm amplitudes is pervasive in proteins. For instance, in Figure 1, we show AMBER MD simulated distance fluctuations between the amide proton of Leu6 of GB1 and several other protons. GB1 is a small domain (56 residues) of the Immunoglobulin G-protein. According to the MD simulation, large distance fluctuations occur, even though GB1 is generally characterized as a very rigid protein (5). Such large-amplitude motions, if they would be present in reality, cannot but dramatically affect protein biochemistry (6) (7) and protein entropy (8) (9).

Figure 1. Left: Example of the fluctuations of the Ile6 HN -HA (black), HN-HB (blue), HN-HG (green) and Ile6 HN- Thr51 HB (red) distances in a MD trajectory for GB1 at 283K. Right, the impact of these distance variations on NMR relaxation rates, expressed as (distance)$^{-6}$.

Clearly, in Figure 1, motions as parametrized by distance fluctuations between ^{1}HN and the backbone ^{1}HA are much smaller than those extending into the sidechain (^{1}HN-^{1}HB), while longer distances fluctuate even more. Can we detect such larger motions with experimental techniques?

Experimental support for the "dynamical view" of proteins at the molecular dynamics ns-ps timescale has mostly come from solution NMR spin relaxation experiments (10) and a few solid-state NMR experiments (11). However, these spin relaxation experiments detect only

azimuthal librations of covalently bound pairs of atoms, (e.g. [15]NH-relaxation). It should be of no surprise that the NMR-detected motions using these methods are relatively small (compare the [1]HN-[1]HA variations in Figure 1), especially since distance variations in a covalent pair are negligible. As such these "classic" NMR relaxation studies, suggest that proteins in solution are rather static, while the MD results indicate quite the opposite. Support for the dynamical view of proteins has certainly come from IR vibrational spectroscopy – but these methods are mostly sensitive to vibrations in covalent bonds at a timescale of < 100 fs, and less to dynamics of larger moieties (12). Terahertz spectroscopy detects motions of larger units and provides information on collective modes with < ps time scale (13). Time-dependent fluorescence experiments disclose protein dynamics at the < 5 ns timescale, like NMR spin relaxation, but are limited to the aromatic residues (14). There are a few NMR methods available to sample ps-ns motion beyond the backbone: [2]H and ^{13}C relaxation of methyl groups (9) (15), but these measurements also analyze librations of covalently bound atom pairs and are not sensitive to distance fluctuations. Nevertheless, these measurements disclose much more lively dynamics than the protein backbone (9).

NMR experiments sensitive to distance fluctuations at the ns timescale do exist (NOESY and ROESY) but quantitative interpretation of the cross peaks in terms of actual distances is already difficult (16) (17) (18). We are aware of one study that uses an dynamical ensemble of protein structures, that includes distance variations, to refine NOE crosspeak interpretation.(19) We will discuss this work later.

Figure 1b shows, that if one *could* detect changes in ^{1}H-^{1}H distances by NMR relaxation methods, the impact could be large. This is because NMR relaxation is dependent on the inverse sixth-power of the distance, which is much more variable than the distances themselves. In the example, the [1]HN-[1]HB distance varies by 7%, while the NMR relaxation due to the dipolar interaction between these atoms would vary by 40%.

Here we set out to design and analyze an NMR relaxation experiment that is sensitive to [1]H-^{1}H distance fluctuations. We show that we can precisely measure and analyze semi-selective R_2 (actually R_{1rho}) NMR relaxation rates of the amide hydrogens ([1]HN). These relaxation rates are dominated by [1]HN-[1]HX dipolar interactions, where [1]HX represent all other protons, including other nearby [1]HN. As such, these [1]HN-[1]HX R_2 rates provide information about dynamical phenomena beyond the backbone in the protein. This source of information has not been tapped before. The likely reasons are that the proper NMR experiment did not yet exist, and the

3

interpretation of the rates is hampered by the large number of relaxation terms that contribute (see the Section 2 "Negotiating the complexity of protein R_2 ^{1}HN-^{1}HX NMR relaxation").

4

We have measured the semi-selective R_{1rho} rates for the small protein GB1 (56 residues) at 283 and 303 K. Several crystal structures are available for GB1; we used the hybrid solid-state NMR - crystallography entry 2qmt.pdb with a resolution of 1.05 Å (20). We wrote a computer program to calculate theoretical theoretical R_{1rho} rates from this structure and found the correspondence with experimental data very poor, even after "minimization" of the structural coordinates (see Results). This is not a surprise: proteins are not rigid, and dynamical variations in ^{1}HN-^{1}HX distances should greatly affect the ^{1}HN relaxation (e.g., see Figure 1b). We proceeded by preparing a suite of computer programs to calculate theoretical R_{1rho} rates incorporating fluctuating distances and angles as obtained from long (200 ns) MD simulations, using the crystal structure as a starting point. Incorporating dynamics in the calculations provided a significant improvement in the agreement with experiment, although the correlation is still not as strong as we would like. Nevertheless, we interpret the improvement as a demonstration of the existence of extensive dynamics in the protein. As an aid to analysis, we also compute ^{1}HN-^{1}HX order parameters. these are significantly smaller than the "classical" HN-N order parameters, which do not report on distance fluctuations.

Again, why was such an NMR analysis not available before? This is most likely due to the fact that the analysis of the NMR data is indeed quite complicated. In the following section, we will describe these complications, and how we navigated around them. This section may be skipped by non-NMR experts, who will nevertheless be able to appreciate the improvement in data fitting when we include dynamics; the latter is presented in the Results.

5

2. Negotiating the complexity of protein R_2 ^{1}HN-^{1}HX NMR relaxation

2.1 Proton transverse (R_2) relaxation in proteins is affected by many factors (21). These comprise dipole-dipole interactions with other nuclei, chemical shift anisotropy relaxation, interference of relaxation mechanisms (22), and conformational exchange broadening (23), including exchange with water and scalar couplings. This complexity has led the avoidance of these sorts of measurements, although labeling strategies involving partial deuteration have been explored, producing isolated ^{1}H spins at significant numbers of backbone and sidechain positions (24). The change in proton R_2 rates as a function of a paramagnetic probe can be used to map electrostatic potentials near proteins (25) (26), and this application has led to some renewed interest in proton R_2 measurements.

We here show that when using a specialized R_{1rho} experiment (27), many of the complexities can be avoided. At the outset, it should be mentioned that these R_{1rho} relaxation rates cannot be interpreted without knowledge of the structure. Even then, one of the problems immediately presenting itself is that NMR dipole-dipole interactions are different for "like" spins and "unlike" spins (28). When the two interacting spins have exactly the same chemical shift, the interaction is "like", while when the shifts are different beyond the linewidth, they are "unlike". The intermediate case obeys a complicated equation that also depends on the linewidths (29). Precise knowledge of *both* the NMR spectrum and the structure are thus a prerequisite to interpreting the relaxation rates. All ^{1}HN relaxation rates are also affected by (potentially anisotropic) rotational diffusion, and by conformational exchange broadening, including mass exchange with water.

The R_2 *measurement* is complicated by (unresolved) scalar couplings with other nuclei. Not only are partially resolved scalar couplings difficult to deconvolute from the true R_2 rate, but the associated in-phase / anti-phase oscillations bring R_1 relaxation of the coupled spin into account, which in turn can be either "selective" or "unselective" (25). It thus may seem that protein R_2 measurements and their interpretations are too convoluted for use.

These complicating issues have long been realized by Bodenhausen and co-workers (21) (30). They developed methods in which selective pulses excite just one proton resonance at a time, followed by a selective low-power spinlock. During the following signal decay (R_{1rho}), scalar couplings with all other spins are eliminated, chemical exchange broadening is suppressed, and the dipolar interactions are all between "unlike" spins. However, elegant and precise as it is, this method can hardly be used for a comprehensive measurement of ^{1}HN relaxation rates in proteins, especially larger ones.

6

2.2 Here, we extend the methods pioneered by Bodenhausen and develop a method that captures R_2 rates for *all* amide protons in a protein at once. Figure S2 in the supplemental information shows the pulse sequence of a novel semi-selective R_{1rho} -HSQC experiment. We make use of the spectral separation of amide protons and aliphatic protons to selectively excite all the amide protons at once. Subsequent application of a high-powered spinlock will just lock the excited spins, which, besides amide protons, also comprise aromatic protons and in principle, the exchangeable protons from Asn, Gln, Ser, Arg, Lys and Thr residues. The result is that all proton pairs that were selectively excited, have during the spinlock identical chemical shifts (that of the spinlock frequency) and are thus "like" protons (31) while all other protons are "unlike". As the scalar coupled $^1H_{alpha}$ protons are not locked (since they were not excited in the first place), the $^3J_{HNHA}$ is decoupled (for TOCSY effects, see below).

The measured relaxation rate R_M is given by (32):

$$R_M = k_{ex} + R_{1rho}\cos^2\theta + R_1\sin^2\theta + \cos^2\theta \; \frac{p_A p_B (\omega_A - \omega_B)^2 (k_{AB} + k_{BA})}{(k_{AB} + k_{BA})^2 + \omega_{eff}^2} + R_2^{HN-N} + R_2^{HN-CSA} + R_2^{HN-C} \quad [1]$$

Here, R_{1rho} is the transverse relaxation rate under infinite-power spin-lock, while R_1 is the longitudinal relaxation. The other terms in Eq [1] will be defined and discussed in the paragraphs below.

2.3 Let us consider the first term, which is the k_{off} rate of the amide-bound proton *H'* in the proton mass exchange process

$$H'N + HOH \xrightarrow{koff} HN + HOH' \quad [2]$$

The intrinsic (unprotected) amide proton exchange rate is given by the empirical relation (33) :

$$k_{ex} = \frac{\ln 2}{200}\left[10^{pH-3} + 10^{3-pH}\right] \times 10^{0.05T} \quad [3]$$

From the experimental parameters of the spectra (pH 6.5 , 10 °C and 30°) we calculate 0.6 and 10 s^{-1} exchange rates, respectively. However, the amide protons are protected from exchange through hydrogen bonding and due to inaccessibility. The following relationship quantifying these protection factors *P* has been developed by (34)

$$P = exp\left(0.34N_C\right) \times exp\left(1.9N_H\right) \quad [4]$$

7

Where N_C is the number of "heavy" atoms surrounding the amide nitrogen within 6.5 Å, and N_H the number of hydrogen bonds per amide proton. The coefficients were obtained by (35).

Applying Eq [4] to the structure 2qmt.pdb, we obtain protection factors varying between 2.6 x10^{10} and 3.8x10^4 . According to these equations, the amide proton exchange rates (Eq 1] are reduced by these very large protection factors.

Summarizing, the maximum rate is 10 / 3.8x10^4 = 2.6x10^{-4} s^{-1}occurring for amides in loops at 303 K. Hence, the life-time broadening of the amide proton resonances as listed as k_{ex} in Eq. [1] can be neglected for all amide protons.

2.4 Let us estimate the relative contributions of the second and third term of Eq [1] for our experiments. These terms describe resonance-offset effects, with the θ being the angle of the spinlock field with respect to the locking axis:

$$\theta = \tan^{-1} \frac{\triangle \omega}{\omega_{rf}}$$

[5]

Here $\triangle \omega$ is the offset between the spin-lock carrier and the resonance of interest, and ω_{rf} the field strength of the spinlock.

For GB1, the maximum offset between the spin-lock carrier at 8.5 ppm and the amide resonances is 1.87 ppm, or 1120 Hz with the used 600 MHz spectrometers. We used a spinlock fields of 12.6-14 KHz. Hence the values for the largest offsets are $cos^2\theta$ = 0.99 and $sin^2\theta$ = 0.01. Without other terms we have R_M=0.99 R_{1rho} for all resonances, and the third term in Eq [1] can be neglected.

2.5. Equation [1] also describes with the fourth term the effect of the spinlock field on a (putative) fast exchange broadening for an individual resonance between two frequencies ω_A and ω_B, populations p_A and p_B, and the (pseudo) first-order rate constants k_{AB} and k_{BA}. The effective spinlock field in this equation, ω_{eff} is given by

$$\omega_{eff} = \sqrt{\omega_{rf}^2 + \triangle\omega^2} \cong \omega_{rf}$$

[6]

since $\omega_{rf} >> \triangle\omega$ (see above).

A complete suppression of the (putative) broadening will occur if

$$\omega_{rf} >> k_{AB} + k_{BA}$$

8

No effect of the spinlock will occur if $k_{AB} + k_{BA} >> \omega_{rf} \cong 6x10^4 \, rad.s^{-1}$

Thus, we may state that all conformational exchange processes with kinetics (much) slower than 10^4 s^{-1} will be suppressed by the spinlock. Variation of the spinlock field strength may uncover exchange processes in that 10^4 s^{-1} time range.

2.6 In total, we have that R_M, for the vast majority of cases is given by the second term R_{1rho} in Eq [1]. But we still need to make a distinction between "like" and "unlike" spins. Classically, "like" spins are those who have exactly the same "natural" resonance frequency. But in a spin-lock experiment, all locked resonances have the same frequency, i.e., that of the spinlock. In that case we have:

(27),(29) (31):

$$R_{1\rho} = \frac{1}{20}\left(\frac{\mu_0}{4\pi}\frac{\gamma_H\gamma_H\hbar}{r_{HH}^3}\right)^2 \times \left\{\frac{9\tau_c}{1+\omega_{eff}^2\tau_c^2} + \frac{15\tau_c}{1+\omega_H^2\tau_c^2} + \frac{6\tau_c}{1+\left(2\omega_H\right)^2\tau_c^2}\right\} \qquad [7]$$

$\mu_0, \gamma_H, \hbar$ are the magnetic permeability of vacuum, the proton gyro-magnetic ratio and Planck's constant divided by 2π, respectively.

r_{HH}, τ_c, ω_H are the ^{1}HN-^{1}HX proton distance, the rotational correlation time (assuming isotropic tumbling) and the proton resonance frequency, respectively. In our application, $\omega_{eff}^2\tau_c^2 << 1$ and Eq. 7 becomes the "like" R_2 spin relaxation rate equation:

$$R_2 = \frac{1}{20}\left(\frac{\mu_0}{4\pi}\frac{\gamma_H\gamma_H\hbar}{r_{HH}^3}\right)^2 \times \left\{9\tau_c + \frac{15\tau_c}{1+\omega_H^2\tau_c^2} + \frac{6\tau_c}{1+\left(2\omega_H\right)^2\tau_c^2}\right\} \qquad [8]$$

The "unlike" relaxation rate is given by (27), (31):

$$R_{1\rho} = \frac{1}{20}\left(\frac{\mu_0}{4\pi}\frac{\gamma_H\gamma_H\hbar}{r_{HH}^3}\right)^2 \times \left\{\frac{5\tau_c}{1+\omega_{eff}^2\tau_c^2} + \frac{9\tau_c}{1+\omega_H^2\tau_c^2} + \frac{6\tau_c}{1+\left(2\omega_H\right)^2\tau_c^2}\right\} \qquad [9]$$

Which for our conditions becomes the "un-like" R_2 spin relaxation rate equation (29):

$$R_2 = \frac{1}{20}\left(\frac{\mu_0}{4\pi}\frac{\gamma_H\gamma_H\hbar}{r_{HH}^3}\right)^2 \times \left\{5\tau_c + \frac{9\tau_c}{1+\omega_H^2\tau_c^2} + \frac{6\tau_c}{1+\left(2\omega_H\right)^2\tau_c^2}\right\} \qquad [10]$$

9

2.7 The spinlock fields, employed for the purpose of suppressing the $^3J_{HNHA}$ scalar coupling and exchange broadening, may, in principle, also cause coherence transfer (TOCSY (36) or HOHAHA (37)) from the amide protons to the scalar coupled alpha protons, which would result in sinusoidal perturbations of the relaxation curves. However, since the spinlock carrier has been placed down field (8.5 ppm) of *both* HN and HA resonances, the transfer is completely negligible (see density matrix calculations based on the strong-coupling spin Hamiltonian in the Appendix).

2.8. According to our analysis above, the measured relaxation rates R_M in Eq. 1 are to within 1% identical to the R_2 rates in Eq. [8 and 10], extended by the dipolar relaxation of ^{1}HN with ^{15}N, ^{1}HN with ^{13}C and the CSA relaxation for ^{1}HN. But, the expressions [8] and [10] above refer to single proton pairs only. Even in small proteins, many protons interact magnetically. There are typically 100 protons in an 8 Å sphere around an amide proton which all contribute to the ^{1}HN relaxation. All these dipolar-dipolar interactions will *interfere* with each other (cross correlation) (22,38,39). For example, an amide proton *i* in dipolar interaction with two other protons *k* and *l* will exhibit two different relaxation rates, $R_2^{i,k} + R_2^{i,l} \pm CC_{DD}^{ik,il}$. (22,38,39) The amplitude of the cross-correlation (CC) term is dependent of the geometry of the three-spin triangle (22,38,39) and can vary between 0 and $R_2^{i,k} + R_2^{i,l}$. Similar interference is the case for all of the many three-spin triangles the "center" spin *i* is involved in.

This appears to be an impassable hurdle towards interpretation of the ^{1}HN-^{1}HX relaxation rates. Fortunately, this is not such a big issue after all. If one fits a single exponential to the beginning of the relaxation curves only, the CC terms cancel since the average of

$$exp\left(-\left(R_2 + CC\right)t\right) + exp\left(-\left(R_2 - CC\right)t\right) \cong exp\left(-R_2 t\right)$$

[11]

for $t << 1/R_2$.

In a recent paper, we showed that this approximation also holds when many relaxation pathways interfere (40). Actually, the interference of multiple relaxation terms cancels better than for just a few terms.

Thus, we have, when fitted from the beginnings of the relaxation curves, that *N* other protons *j* for an amide proton *i* will co-add in a simple pair-wise manner:

$$R_2^{i-total} = \sum_{j \neq i}^{j=N} R_2^{ij}$$

[12]

10

2.8. In our computations we use a value of 9.7 ppm for the ^{1}HN CSA, assuming axial symmetry. This value was taken from (41). With that, one calculates that on average the ^{1}HN chemical shift anisotropy relaxation accounts for 4 % of the total amide proton R_{1rho} (at 600 MHz). The same authors also show that the ^{1}HN CSA varies by +/- 22% (in ubiquitin) and that that variation is strongly correlated with the ^{1}HN isotropic chemical shift. Such a variation in CSA will account for almost 50% in the ^{1}HN CSA relaxation, since the latter depends on the square of the CSA. But this amounts to just an uncertainty of 2% in the overall ^{1}HN relaxation. We decided this difference is too insignificant as to incorporate a variable CSA in our calculations. However, if the R_{1rho} experiments were to be carried out at higher fields (see below) one would have to bring this into account.

2.9. Last, but not least, since the vectors connecting the different pairs ^{1}HN-^{1}HX will point in many different directions, the influence of anisotropic molecular diffusion (42) on the rates will be averaged out.

In the end, our calculations suggest that the decay of the spin-locked ^{1}HN coherence (R_M) is given by the dipolar ^{1}HN-^{1}HX interactions (on average 67% of the total rate), the dipolar interaction with the attached ^{15}N (24%) , dipolar interaction with ^{13}C nuclei (on average 5%) , and by ^{1}HN chemical shift anisotropy relaxation (4 % at 600 MHz) .
Water molecules that are bound to the protein with large residence times can also contribute, but we have not considered this complication here.

In this work, rather than attempting to make any direct decomposition of the total rates into the individual terms in Eq. [12], we compute the sum from results of molecular dynamics simulations and explore the sorts of information that can be extracted by comparing these to the measured rates.

11

3. Results.

For GB1, shown in Figure S1, we find that the R_{1rho}-HSQC experiment (Figure S2) can obtain site-resolved R_{1rho} relaxation rates for individual ^{1}HN resonances with high precision Figure S3 and Table S1 and S2). Representative decay curves are given in Figure S3.

For GB1, the experimental R_{1rho} data could be fitted well with a single exponential, often with a RMSD of fit of less than 3% (see Figure S3). A Table with the obtained rates and their error estimations is provided in the SI. (Tables S1 and S2). In Figure S4, we compare the R_{1rho} rates for two values of the spinlock power, 6 and 12 kHz. The rates are equal withing the error ranges, except for 8 residues , where the rate is significantly faster with the smaller spinlock field-strength. This indicates that these HN experiences conformational exchange broadening with a rate around 104 s^{-1}. Most, but not all, of these protons are found in loops (see Figure S1)

Without local motion or exchange broadening, the theoretical relaxation rates are dependent on just two parameters (e.g., see Equations 8, 10 and 12) : the ^{1}HN-^{1}HX distances as obtained from the (crystal) structure, and the protein rotational correlation time τ_c. We experimentally determined the latter from "classical" ^{15}N relaxation studies (R_1, R_2 and NOE) (43) (10) (44) at 10 ^{0}C using the same sample as used for the R_{1rho} experiments at 10 ^{0}C. We obtained an average value of 5.96 ns, taking anisotropic diffusion into account (minimum 5.62 ns maximum 6.63 ns). This value corresponds reasonably well to the average value computed from the crystal structure 2qmt.pdb using the program HydroNMR (42) (6.4 ns, average of the anisotropic eigenvalues) while the empirical equation developed by Daragan et al. yields 7.0 ns (45). We will proceed here by discussing the results and computations at 283K. The experiments and calculations at 303K yield the same overall picture and will be discussed later.
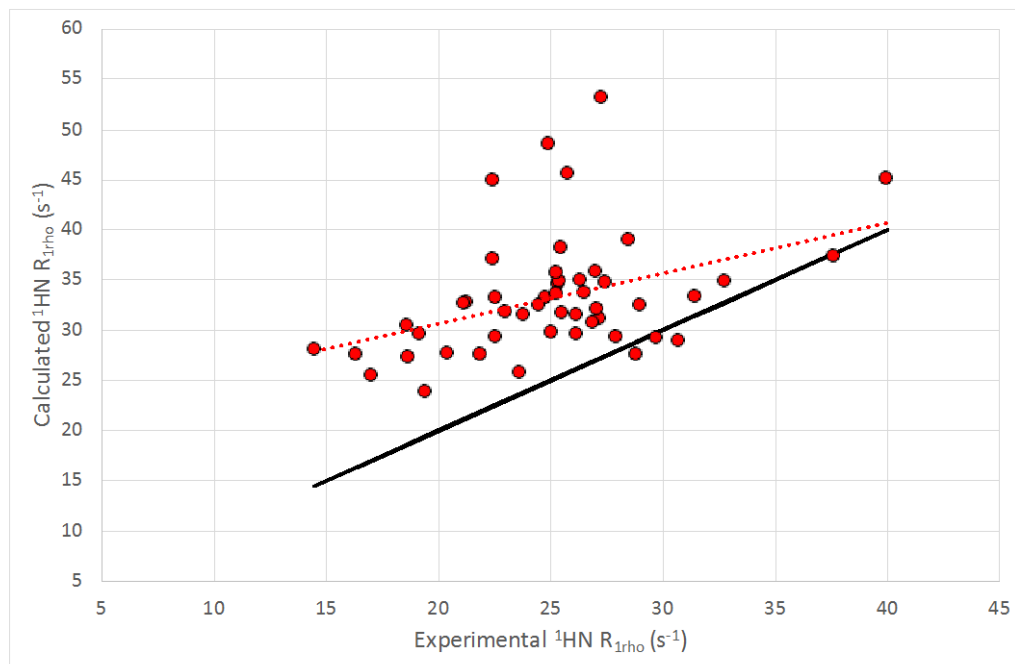
12

Figure 2. Calculated vs Experimental R_{1rho} rates (Eqs. 8,10 and 12). The calculation is based on the structure 2qmt.pdb and the experimental rotational correlation time, τ_c = 5.96 ns. The black line shows y=x.

When using the experimental rotational correlation time τ_c of 5.96 ns, the average computed R_{1rho} relaxation rate at 283 K was 33.9 s^{-1}, which is much larger than the average experimental rate of 25.1 s^{-1} (see Figure 2 and Table 1, rows 1 and 2). It thus seems that the experimental ^{15}N correlation time might be too large to be used for the ^{1}H-^{1}H relaxation computations. The difference is even larger when using the HydroNMR correlation times. But it must be unlikely that the correlation times can be that far off; rather, the mismatch is the first indication that the ^{1}H-^{1}H relaxation dipoles are more susceptible to local motion and have smaller order parameters than the ^{15}N-^{1}H dipoles.

13

	TABLE 1									
ROW	Calculation	TEMP	τ_C	AVERAGE[a]	SCALING[b]	RMSD[c]	RMSDR[d]	PEARSON-R[2][e]	SLOPE[f]	R-FACTOR[g]
		K	ns	s-1		s-1	%			%
1	Experiment	283	5.96	25.1		0.51	2			
2	XRAY	283	5.96	33.9	1	6.65	20	0.22	0.50	35
3	XRAY	283	5.96	25.1	0.74	4.33	17	0.22	0.37	14
4	MINIMIZED	283	5.96	25.1	0.76	4.65	19	0.20	0.42	14
5	MINIMIZED ANISOTROPIC	283	5.96	25.1	0.76	4.64	19	0.16	0.38	15
6	DYNAMIC AVERAGE	283	5.96	25.1	0.74	5.23	21	0.07	0.32	16
7	FULL DYNAMIC (4A)	283	5.96	25.1	0.94	4.30	17	0.36	0.47	13
8	FULL DYNAMIC (5A)	283	5.96	25.1	0.88	4.24	17	0.47	0.52	11
9	FULL DYNAMIC (6A)	283	5.96	25.1	0.87	4.22	17	0.48	0.52	11
10	FULL DYNAMIC (7A)	283	5.96	25.1	0.87	4.21	17	0.48	0.52	11
11	FULL DYNAMIC(8A)	283	5.96	25.1	0.86	4.21	17	0.50	0.52	11
12	FULL DYNAMIC(9A)	283	5.96	25.1	0.85	4.21	17	0.51	0.52	11
13	FULL DYNAMIC*	303	5.96	25.1	0.88	4.27	17	0.52	0.5	11
14	Experiment	303	3.6	15.1		0.14	1			
15	XRAY	303	3.6	22.1	1	4.37	20	0.51	0.89	45
16	XRAY	303	3.6	15.1	0.65	2.19	15	0.51	0.58	11
17	MINIMIZED	303	3.6	15.1	0.68	2.4	16	0.41	0.66	11
18	MINIMIZED ANISOTROPIC	303	3.6	15.1	0.70	2.39	16	0.38	0.63	13
19	DYNAMIC AVERAGE	303	3.6	15.1	0.69	2.47	16	0.14	0.40	12
20	FULL DYNAMIC (8A)	303	3.6	15.1	0.82	2.17	14	0.76	0.72	6

14

Legend to Table 1:

Summary of experimental and calculational statistics of GB1. The row numbers are quoted in the text. The experiments were carried out at two temperatures. The rotational correlation time, τ_c was determined experimentally at 283K from ^{15}N relaxation rates. The value of τ_c at 303K was extrapolated from the former using viscosity tables.

(a) Averages over residues 4-53. (b) The scaling factor used to obtain the best correspondence between the average of the calculated rates and the experimental rates.

(c) Root-Mean Square Deviations; for the experiments these are the averages of the experimental uncertainties (See SI); for the calculations these are the standard deviation of the differences between experimental and calculated values. (d) Ratio of RMSD and the average. (e) Square of the Pearson correlation coefficient (f) slope of the linear least-squares fit. (g) R-factor as commonly used in the crystallographic literature (46)

The calculations "XRAY" are from the static coordinates 2QMT.pdb (47) , and are the sum of the ^{1}HN-^{15}N, ^{1}HN-CSA, ^{1}HN-^{13}C rates, ^{1}HN-^{1}HX R_{1rho} (R_2) relaxation rates. The calculations "MINIMIZED" are from the static coordinates 2QMT.pdb, energy minimized with the AMBER 1ff19SB forcefield (48). The calculations "MINIMIZED ANISOTROPIC" correct the ^{1}HN-^{15}N, ^{1}HN-CSA rates for rotational diffusion anisotropy, as calculated from HydroNMR (42). The calculations DYNAMIC are the sum of the static values of isotropic ^{1}HN-^{15}N, ^{1}HN-CSA multiplied with ^{1}HN-N order parameters, static values of ^{1}HN-^{13}C multiplied with ^{1}HN-^{13}C sum-order parameters, and the dynamical ^{1}HN-^{1}HX R_{1rho} relaxation rates. The value in parenthesis indicates the radius of the sphere limiting the selection of ^{1}HN-^{1}HX distances for to be extracted from the MD simulations. The relaxation rates were extracted from a 200 ns MD trajectory at the indicated temperatures. The calculation "DYNAMIC*" compares the experimental values at 283 K with a computation a rotational correlation time of 5.96 ns, belonging to the 283K temperature, but used order parameters and dynamical dynamical ^{1}HN-^{1}HX R_{1rho} relaxation rates from the 303K MD trajectory.

In order to fit to the experimental average, we reduced all computational rates by a factor of 0.74 (*i.e.,* a simple approach to obtain an average ^{1}HN-^{1}HX order parameter). The result is shown in Figure 3 and are listed in Table 1, row 3. We improved the fit by multiplying R_{1rho} values due to ^{1}HN -methyl protons interactions by 0.5, in an attempt to account for fast methyl rotation. A

15

justification for this approach is shown in Figure S5, where actual order parameters for such interaction were calculated from a MD trajectory: the average order parameters of short ^{1}HN-CH$_3$ interactions is 0.5. While order parameters for more distant ^{1}HN-CH$_3$ pairs will be larger, we argue that the distant pairs contribute less to the overall R$_{1rho}$ to make the error negligible.
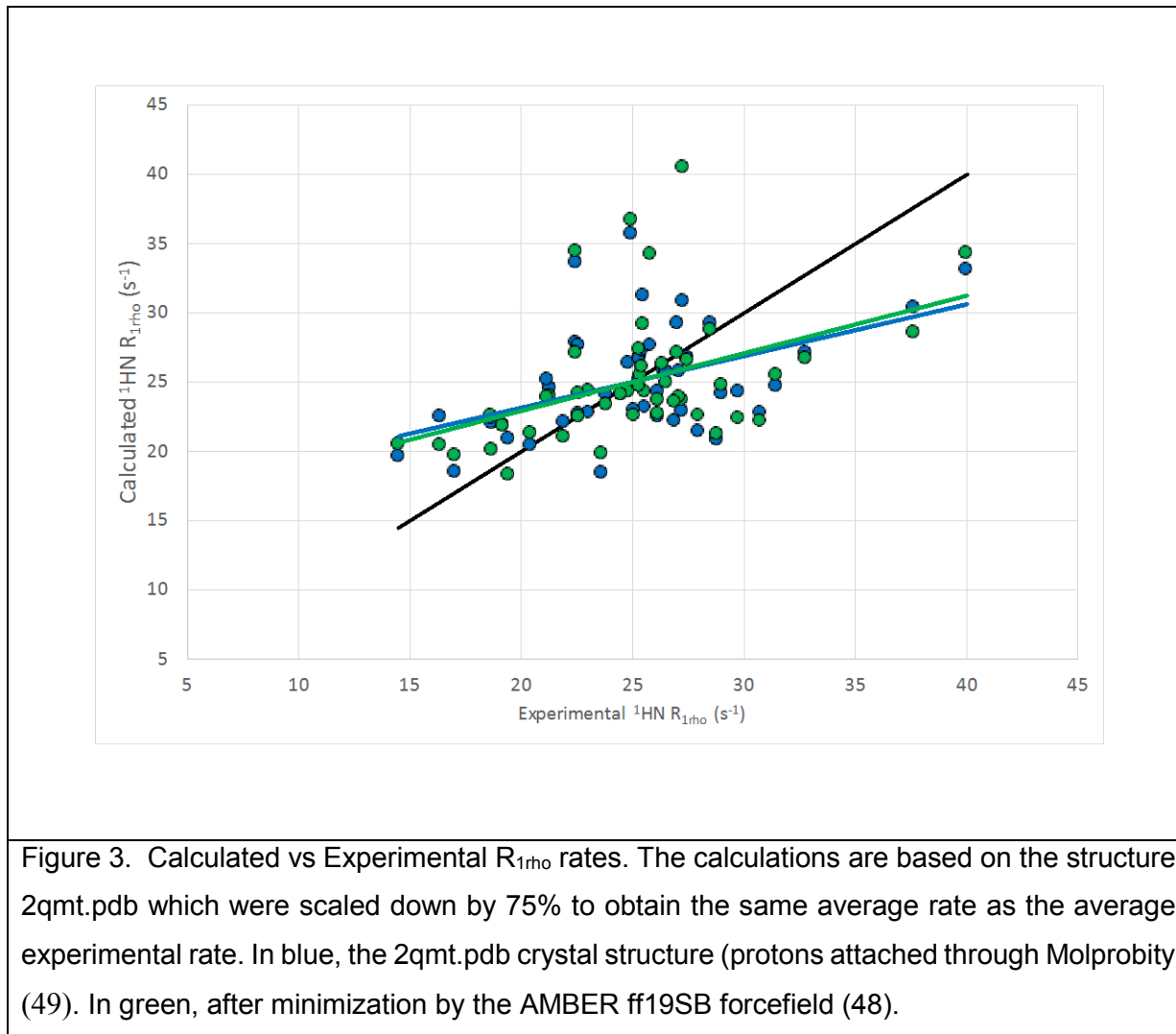

Figure 3. Calculated vs Experimental R$_{1rho}$ rates. The calculations are based on the structure 2qmt.pdb which were scaled down by 75% to obtain the same average rate as the average experimental rate. In blue, the 2qmt.pdb crystal structure (protons attached through Molprobity (49). In green, after minimization by the AMBER ff19SB forcefield (48).
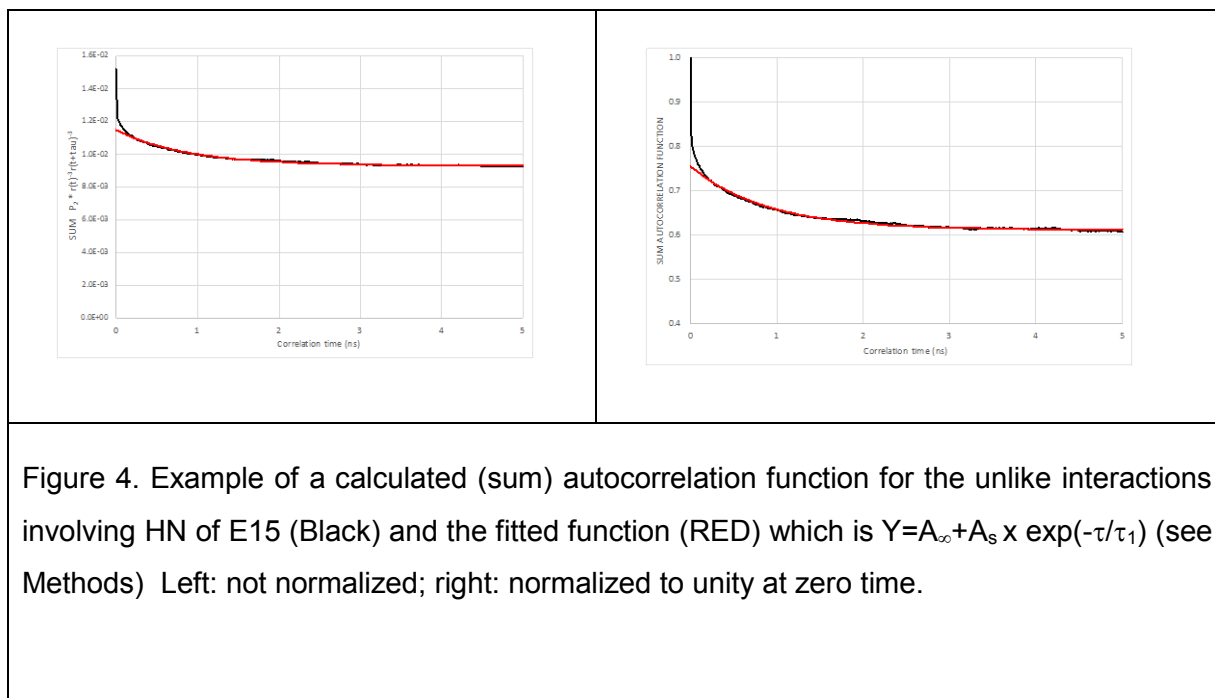
In our computations we experimented with how to treat the interactions of the ^{1}HN with the exchangeable protons. Which exchangebles are spinlocked, and which ones are not? Calculations with different assumptions made no significant difference (results not shown) , and we opted for a common-sense approach to treat interactions with exchanging hydroxyl protons, Lys E-NH$_3$, Arg guanidinium protons, which exchange faster with water than the timescale of the spinlock and which are invisible in the NMR spectrum, as "unlike" interactions, while the sidechain ^{1}HD of Arg, and sidechain NH$_2$ of Asn and Gln, typically visible in the NMR spectrum,

16

were treated as "like" interactions. As the NMR experiments were carried out with a sample in a 95/5 % H_2O/D_2O solution, we reduced all ^1HN-^1H-N and ^1HN-^1HX exchangeable rates by 5%. Despite all of this care, we obtain a Pearson R^2 of just 0.22 and a slope of the fitting line of 0.37 (which should be 1 for a perfect fit). Extensive minimization of the crystal structure coordinates using the AMBER program did not change the quality of the fit (see Table 1 and Figure 3), neither did the explicit incorporation of rotational anisotropy as obtained from HydroNMR affecting the ^1HN-N relaxation rates (Table 1, rows 3, 4 and 5 at 283K, 11,12 and 13 at 303K).

At this point it is clear that the static structure in the 2qmt crystal cannot account for the observed relaxation rates. We thus decided to incorporate dynamics into our modelling. We used the AMBER package, with the ff19SB forcefield (48), to compute 200 ns trajectories of GB1 in OPC water (50) at 283 and 303 K, with the 2qmt.pdb structure as initial condition (see the Methods section for details.) We also computed average structures from these trajectories, but they yielded worse results than the crystal structure (see DYMAMIC AVERAGE" in Table 1, row 6 and 19). Obviously, using a dynamically averaged structure is not the correct way to handle a dynamic ensemble. Thus, we extended our dynamic calculations towards extracting order parameters, and use these order parameters to reduce the computed relaxation rates (see Methods).

A very substantial change in quality of the fitting occurs when incorporating protein dynamics in this way in the computations. We analyzed a 200 ns AMBER trajectory of GB1 in OPC water, using the ff19SB forcefield. First, the overall molecular motion was eliminated by superposing the MD frames. We calculated the autocorrelation functions (AC) of the angular (azimuthal librations) (as P_2cos) and (as $(r^{-3})^2$) distance (radial) variations of the dipole-dipole vectors between individual ^1HN and individual- ^1HX, as in Eq. [9] below. As detailed in the Methods Section, the Fourier transform of the sum auto correlation function is proportional to the sum of the individual HN-HX relaxation rates.

17

Figure 4. Example of a calculated (sum) autocorrelation function for the unlike interactions involving HN of E15 (Black) and the fitted function (RED) which is $Y=A_\infty+A_s \times \exp(-\tau/\tau_1)$ (see Methods) Left: not normalized; right: normalized to unity at zero time.

The sum AC in Figure 4 shows a fast initial decay within 100 ps, followed by a decay with a time constant of a few nano seconds before a plateau is reached. The plateau value is the major determinant of the R_{1rho} relaxation rates: the relaxation rate is reduced to by S^2HN-HX (the plateau value) due to local motion. Motions with a time constant in the nano-second region increase the relaxation rate by a small amount (see Eqs. 21 and 23).   The ps-time scale motions do not contribute to R_{1rho} relaxation rates. For each sum correlation function, we fitted to the plateau value and to the amplitude and correlation time of the slow decay, as is shown in Figure 4, and use these values in the relaxation equations (see methods). Local motions slower than the molecular rotational correlation time are masked by the latter and cause no additional relaxation. We avoided including such motions in our calculations by evaluating the AC functions in MD trajectories for 6 ns only (but averaged over 200 ns).

The results of the dynamic calculations are shown in Figure 5. The Pearson R^2 of just 0.21 has jumped to 0.36-0.50 while the slope of the least-square fit improved from 0.37 to 0.42 - 0.52, depending on the radius of the sphere limiting the selection of ^{1}HN-^{1}HX distances to be considered

18

for the computations (Table 1, rows 7-12). From the values in the Table 1 one sees that the computations converge around a selection sphere of 8Å.
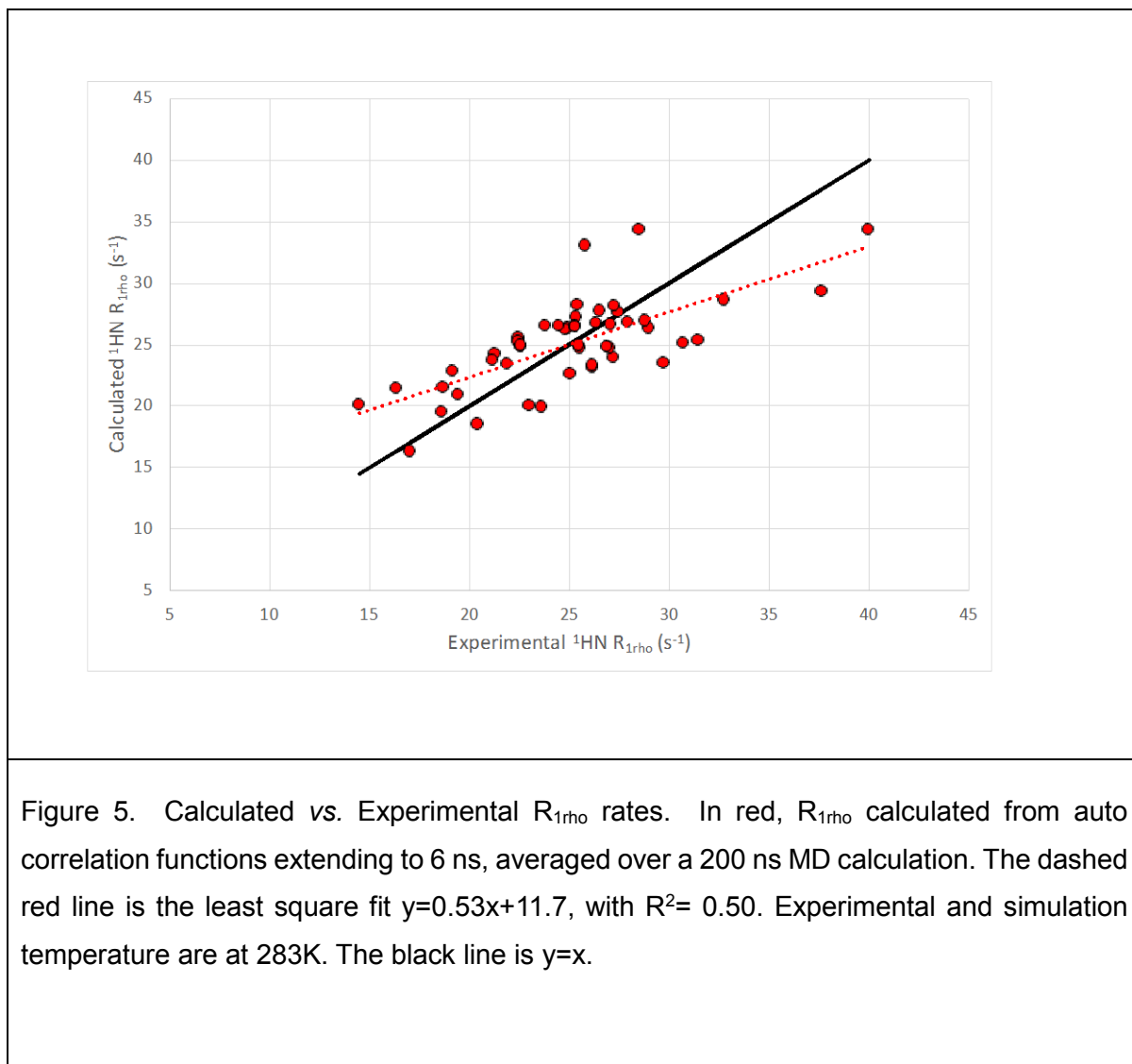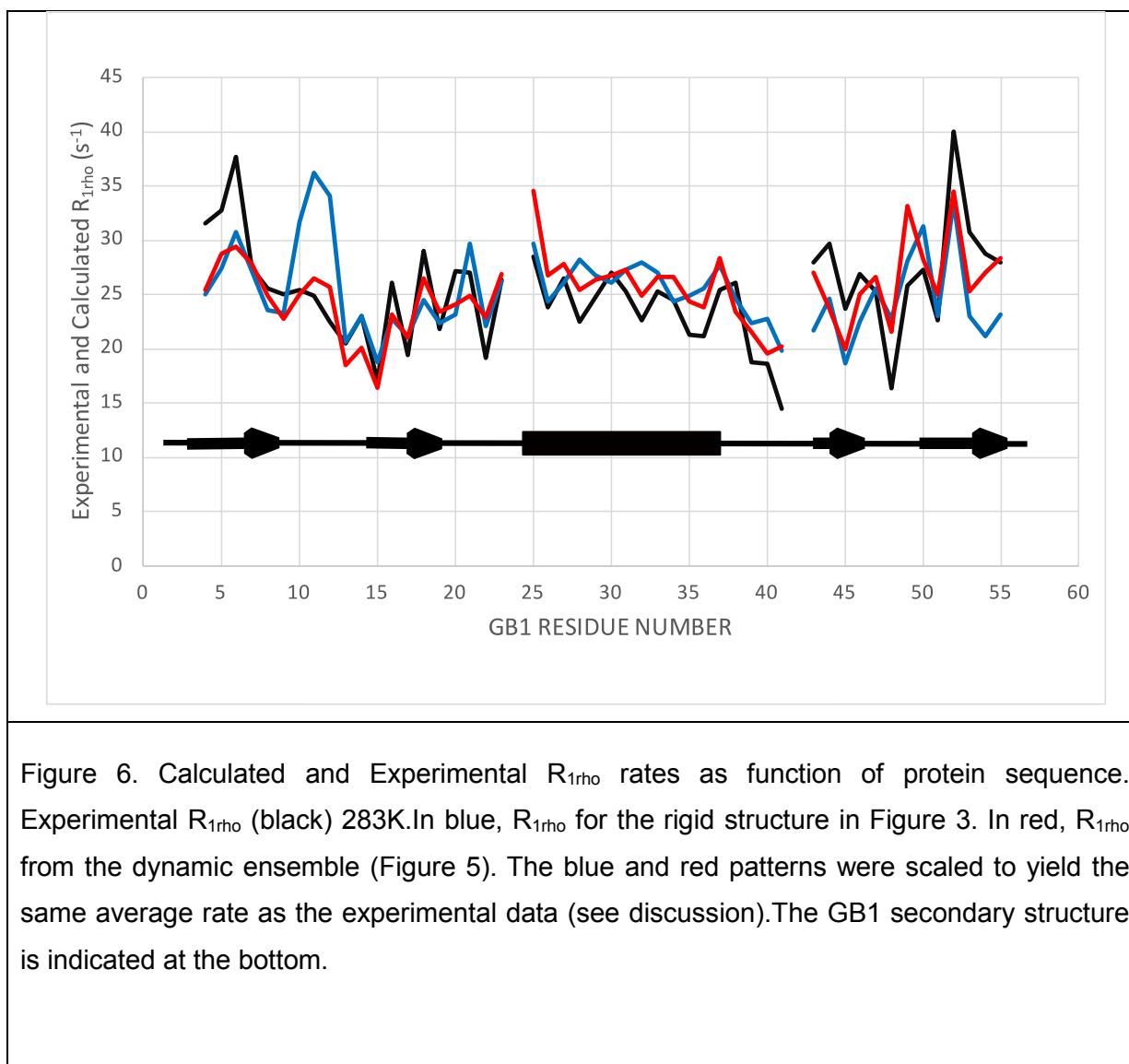

Figure 5. Calculated *vs.* Experimental R_{1rho} rates. In red, R_{1rho} calculated from auto correlation functions extending to 6 ns, averaged over a 200 ns MD calculation. The dashed red line is the least square fit y=0.53x+11.7, with R^2= 0.50. Experimental and simulation temperature are at 283K. The black line is y=x.

From these dramatic improvements it is abundantly clear that the local motion, such as calculated by the MD simulations is indeed detected by the ^1HN-^1HX relaxation rates. Nevertheless, the R^2 of 0.50 is not a very good fit. While dynamics definitely improved matters, there must be other (non-accounted-for) factors that reduce the (calculated) relaxation rates. These will be discussed later.

19

Figure 6. Calculated and Experimental R_{1rho} rates as function of protein sequence. Experimental R_{1rho} (black) 283K.In blue, R_{1rho} for the rigid structure in Figure 3. In red, R_{1rho} from the dynamic ensemble (Figure 5). The blue and red patterns were scaled to yield the same average rate as the experimental data (see discussion).The GB1 secondary structure is indicated at the bottom.

The effect of incorporating dynamics in the calculations is depicted in a different way in Figure 6. Most of the up-down patterns are well-reproduced for both the rigid and dynamic calculation, indicating that the relaxation rates are dominated by the rigid structure. The exception is the helix (residues 25-36): the "phase" of the pattern is off for the rigid computation but is recovered for the dynamic computations. In this figure one also perceives that the large increase in Pearson R^2 occurring when considering dynamics is due to the big change for the loop around residue 11.
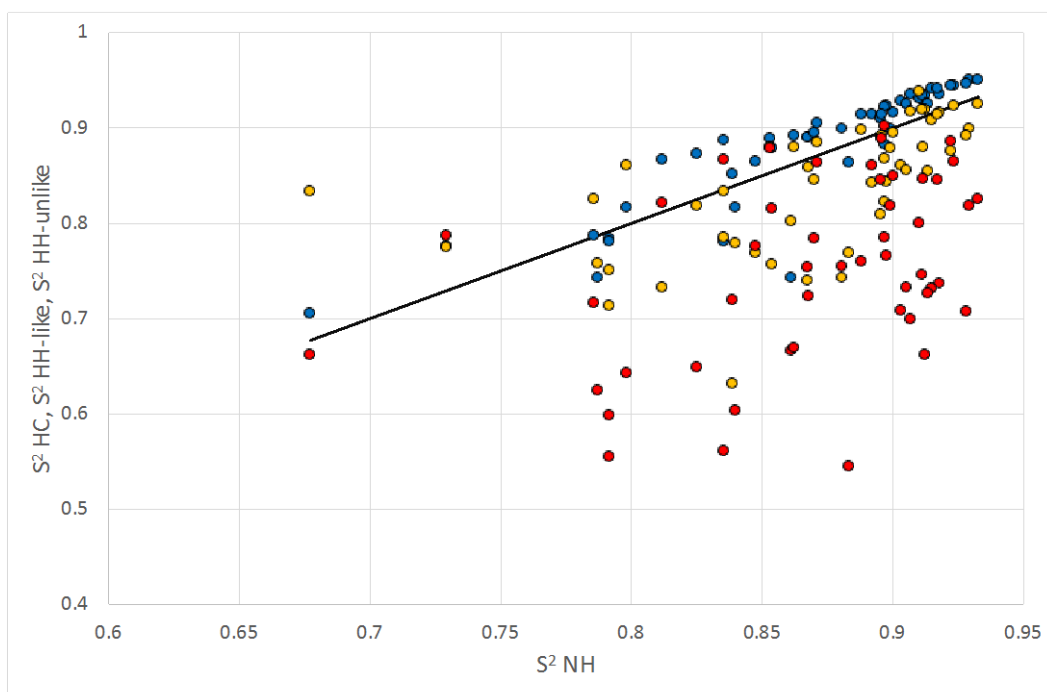
20

Figure 7. The classical S^2NH order parameters (computed) vs the sum S^2HN-HX order parameters for like (yellow) and unlike (Red) interactions. In blue are the sum S^2HN-C order parameters. The black line is y=x. T=283K.

Figure 7 shows that, especially for the unlike spin pairs, the calculated $^1HN-^1HX$ order parameters are (much) smaller than the calculated ^1HN-N order parameters, which correspond to the classical ^{15}NH order parameters.

Figure 8 shows several correlation functions, separating the distance-dependent (radial) and angular auto-correlation functions, for several residues.
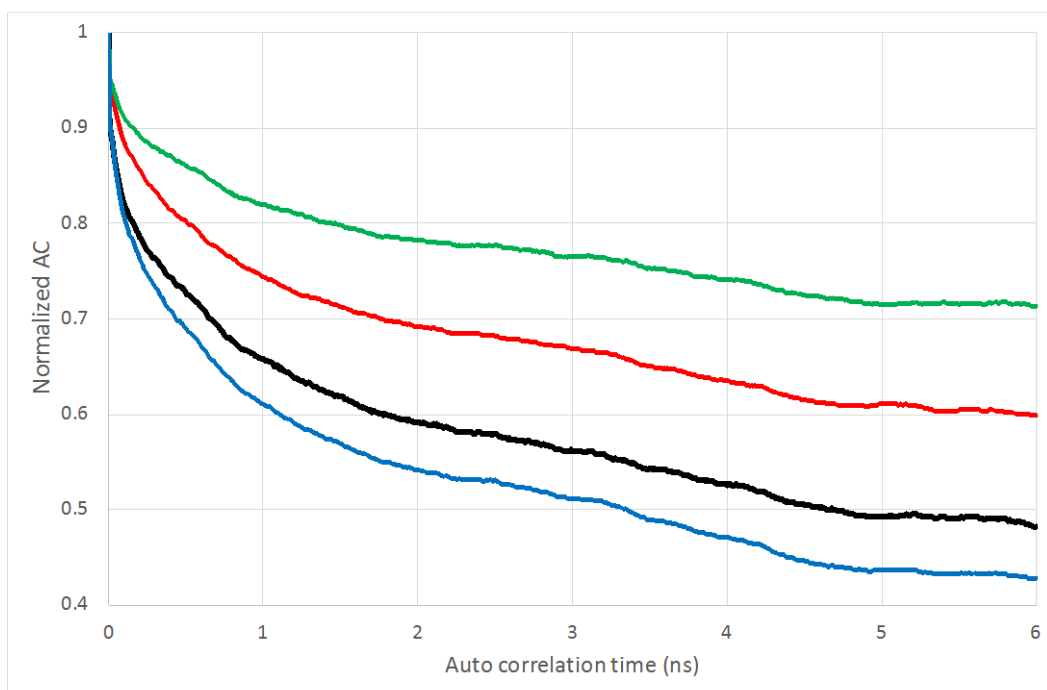
22

23
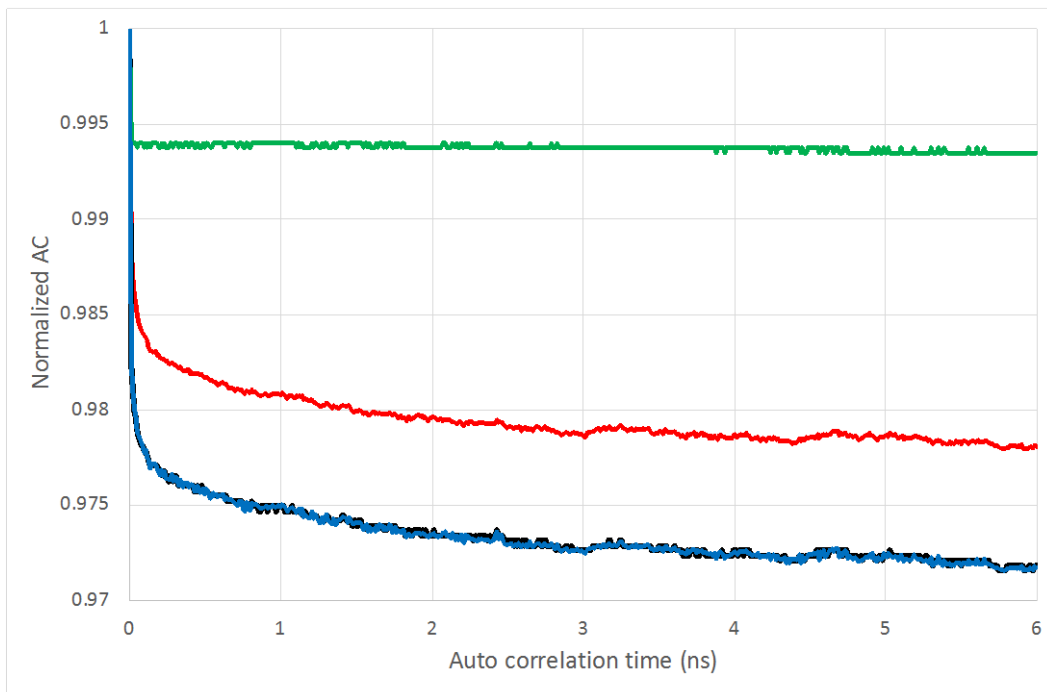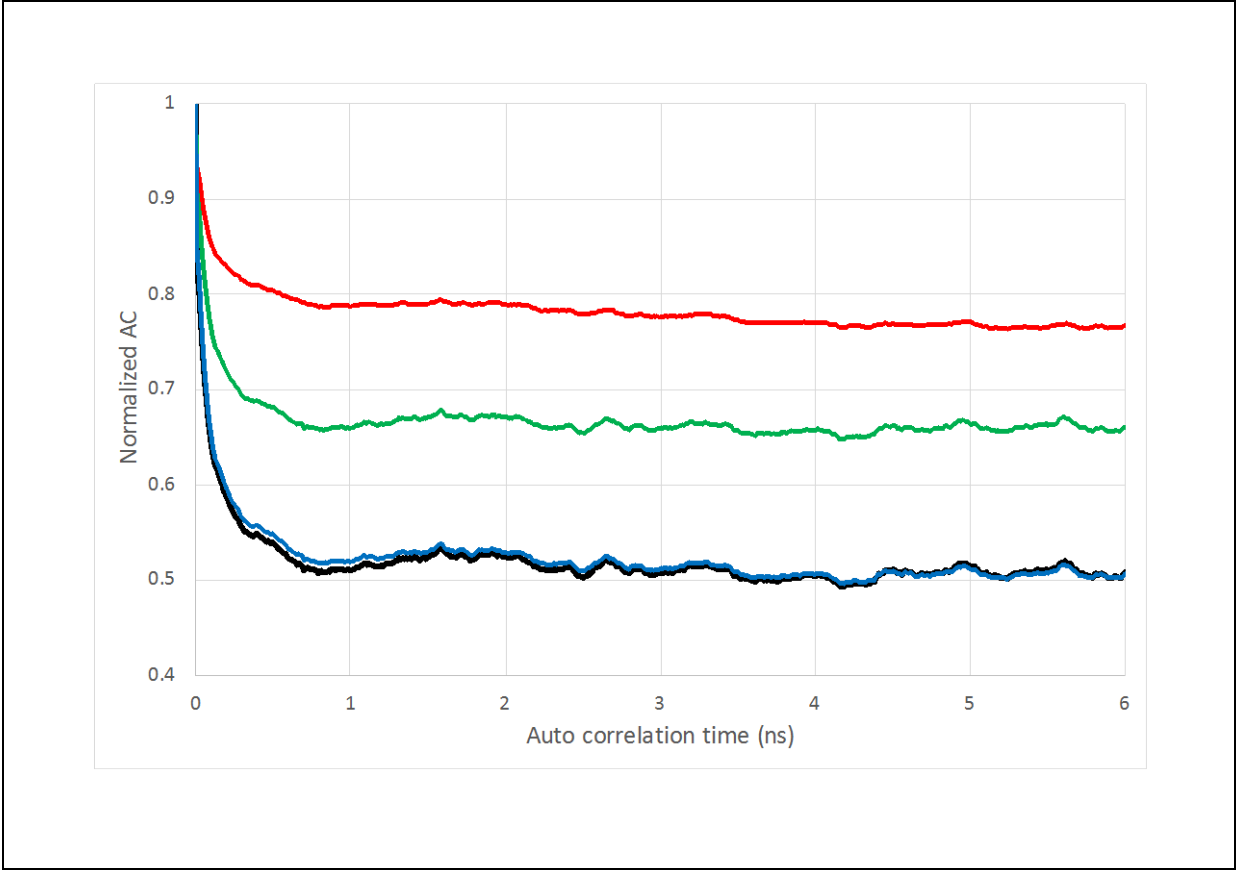
Figure 8. Auto correlation functions as computed from a 200 ns MD trajectory (283K). Top, K31HN-Q32HA; middle, K31HN-K31HG2; bottom, T11HN-L12HG. Note the difference in vertical scale of the panels.

In red, $<P_2(t)P_2(t+\tau)>$; in green, $<1/(r^3(t)r^3(t+\tau)>$;

in blue, $<P_2(t)P_2(t+\tau)><1/(r^3(t)r^3(t+\tau)>$; in black, $<P_2(t)/(r^3(t) \; P_2(t+\tau)/r^3(t+\tau)>$ (used in the computations)

The figure shows that the relative contribution of axial and radial motion to the correlation function, and thus relaxation, is different dependent on the ^{1}HN-^{1}HX vector considered: In the top panel, the angular order parameters, which correspond to the plateau values of the auto correlation functions, are smaller than the radial ones, while both are quite large, indicating little motion. This interaction involves atoms on the backbone (K31 HN-Q 32 HA). The middle panel shows that the radial order parameter can be smaller than the angular order parameter, while in the bottom panel the reverse is the case. The latter two interactions involve sidechain protons, and the motion is quite large. In both latter cases, the overall order parameter for ^{1}HN-^{1}HX comes out significantly lower than the angular order parameters alone. Hence, fluctuations in the interproton distances can contribute greatly to the reduction of the overall relaxation rates.

24

The fact that product of the angular and radial AC's (blue) in the bottom panel is smaller than the product AC (Black) indicates that, in that case, the angular and distance fluctuations are not statistically independent. When the blue and black curves coincide, such fluctuations are independent. In all cases we use $<P_2(t)/(r^3(t) \, P_2(t+\tau)/r^3(t+\tau)>$ in our computations.

The experiments were also carried out at 303K. In the calculations we used a rotational correlation time of 3.6 ns, extrapolated from the value at 283 following viscosity tables. Without taking dynamics into account, the computed R_{1rho} rates were also much larger than the experimental ones (Table 1, row 15). But the Pearson R^2 for the rigid structure was already significantly better ($R^2=0.51$) (see Figure 9a, Table 1, rows 15,16) than at 283K (Figure 3, Table 1 Row 3), and improved further ($R^2=0.76$) by including dynamics, extracted from a MD trajectory at 303 K (Figure 9B, Table 1, row 20). The slope of the linear regression line is also better (0.72). The improvement is also apparent when inspecting Figure 10, where the calculated and experimental rates are depicted versus the protein sequence (compare with Figure 6). Just like at 283K, of the up-down patterns are well-reproduced for both the rigid and dynamic calculations. And, again, the exception is the helix (residues 25-36): the "phase" of the pattern is off for the rigid computation but is recovered in the dynamic computations.
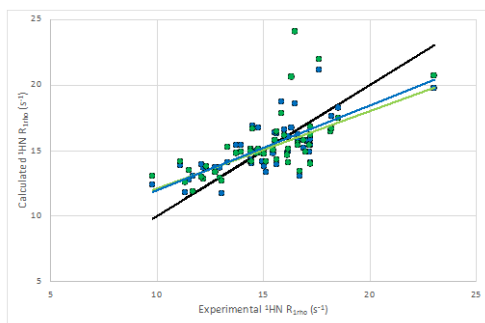
25

Figure 9a.

In blue, experimental R_{1rho} vs R_{1rho} computed from the crystal structure 2QMT.pdb with protons added by Molprobity (Blue). T=303K. In green, after minimization by AMBER. The black line is y=x.

The blue trendline (Xray) is y=0.65x+6.2 with R^2=0.41. The green trendline (Minimized) is y=0.59x+6.2 with R^2=0.51
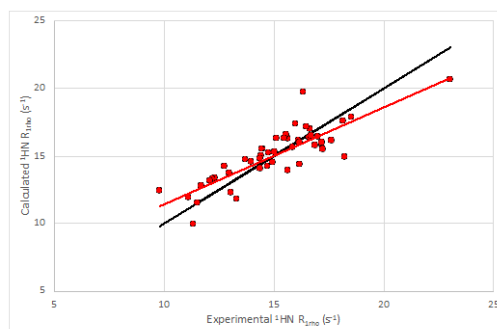
Figure 9b.

In red, R_{1rho} calculated from auto correlation functions extending to 6 ns, averaged over a 200 ns MD calculation. Experimental and simulation temperature is 303K.

The red trendline is y=0.72x+4.3 with R^2=0.71.

The distribution of the order parameters for 303K is found in Figure S5. The distribution is very much like the one at 283K.
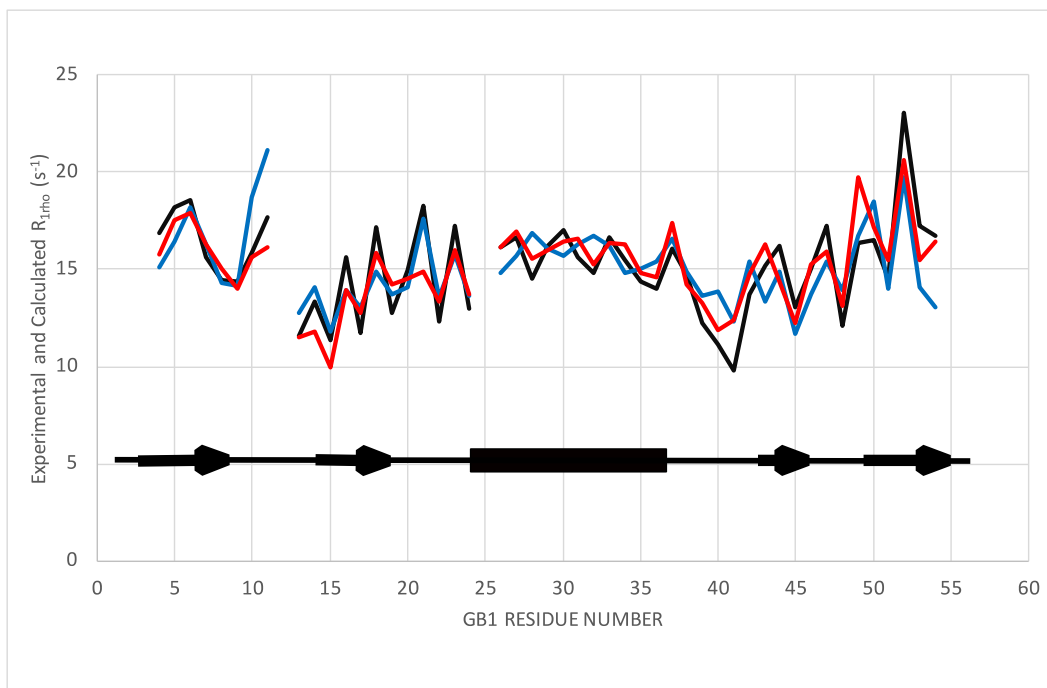
Figure 10.

Experimental R_{1rho} (black) at 303K. In blue, R_{1rho} for the rigid structure in Figure 9a. In red, R_{1rho} from the dynamic ensemble calculated for 303K (Figure 9b). The GB1 secondary structure is indicated at the bottom. Both static and dynamic rates have been scaled so that their mean matches the experimental mean.

27

4. Discussion.

4.1 For a rigid structure, the theoretical ^{1}HN R_2 relaxation rates are just function of the rotational correlation time and the (crystal) structure of the protein (Eqs. [8] and [10]). The rotational correlation time was determined experimentally from ^{15}N relaxation measurements. The latter compares favorably with values computed by the program HydroNMR (42) from the crystal structure. However, the theoretical ^{1}HN-R_2 relaxation rates based on this correlation time are 30% too large as compared to the experiment. (Table 1, rows 2 and 15). In analogy to classical ^{15}N relaxation, these results immediately suggest that local motions with time constants faster than the rotational correlation time, expressed as "modelfree" order parameters, reduce the rates (51). However, the experimental ^{1}HN R_{1rho} rates are subject to so many technical and physical complications, that even while we think address all of them (see results and theory sections) , there remains a gnawing feeling that not all has been covered. But, if a relaxation mechanism was overlooked (say, e.g., dipolar interactions with (bound) waters), the calculated relaxation rates would become even larger than they already are.

What *does* convince us that we are truly measuring dynamical phenomena, is the fact that a dramatic increase in the R^2 of fit occurs when computing R_{1rho} from a dynamical MD ensemble (Table 1 rows 7-12 and 20), and that the radius of the sphere of protons taken into account for the dynamic calculations affects the R^2 factor (see Table 1, rows 7-12).

Figures 7 and S6 show that "unlike" ^{1}HN-^{1}HX vectors, which predominantly correspond to amide-aliphatic vectors are especially dynamic, with order parameters as low as 0.5. Here one should be aware that the ^{1}HN-^{1}HX order parameters report on both angular as well as distance fluctuations (radial order parameters). The "unlike" order parameters are especially low, because many are affected by interactions with fast rotating methyls.

In Figure 8 we separated out the angular and radial autocorrelation functions for a few interactions. One observes very low order parameters (plateau values) for interactions not involving methyl groups as well. Summarizing, we find that the ^{1}HN-^{1}HX R_{1rho} relaxation rates are sensitive to both angular and radial fluctuations, and, in some cases, can be dominated by the radial fluctuations.

The question of how protein dynamics influences homonuclear dipolar relaxation rates is an old one, going back to early days of molecular dynamics simulations, (reviewed, for example in (52)). Most of these studies addressed the effects of motion on individual NOESY or ROESY peaks and used a "static" reference model with the H-H distance taken as the average value from the simulation. With that reference, distance fluctuations increase relaxation rates, rather then

28

decrease them. But, for relaxation, it is not the average distance, but $\left\langle \dfrac{1}{r^6(t)} \right\rangle$ (i.e., AC(0)) that maybe more relevant. With the latter definition, distance fluctuations lead to a reduction of of the relaxation rates, as is required for a better fit with the experiment. Since there is no single structure whose distances all match either <r> or <r^{-6}>$^{-1/6}$, the division between "structural" and "dynamical" contributions to relaxation will inevitably be somewhat arbitrary. The approach used here, using <r^{-6}>$^{-1/6}$ as the reference distance, treats radial and angular fluctuations on an equal footing (see Figure 8) . Griesinger and co-workers are interested in protein structural fluctuations at all time scales. In a recent paper (19), they assume that (all) dynamically accessible states of ubiquitin in solution are represented by an ensemble of 117 static structures available in the Protein Data Bank. The different [1]H-^{1}H distances in these structures contribute to a single NOE cross peak intensity. Rather than just optimizing the populations of these structures and averaging the relevant distances (with the problems as discussed above), they assign interconversion rates between the structures. From these proposed rates, the calculate auto correlation functions relevant to NOE cross peak build-up. They proceed by optimizing the interconversion rates over a large time span (tc +/- 3 orders of magnitude) to obtain a best (collective) fit to the NOE cross peak volumes. The key finding is this dynamic / kinetic approach yields a better fit to the experimental NOE data, than a single structure, or a population optimized non-interconverting (static) ensemble.

Our work, using another approach, thus further confirms the above conclusion that ^{1}H NMR relaxation data (NOE is also relaxation) can disclose underlying protein proton dynamics. Our work is much less detailed than theirs but does not depend on the availability of many (crystal) structures, or high-quality NOE data. Our method can point to an *area* in the protein where dynamical processes are active (rather than individual proton pairs).

While including dynamics *does* improve the R^2, one still needs a scaling factor of 0.85 for a best fit to the average relaxation rates (see Table 1). Is the protein more dynamical than captured in the MD calculations? We investigated if order parameters belonging to a 303K simulation would improve the fit to the 283K data. One indeed does perceive some improvement, (compare Table 1, rows 11 and 16, but it is not sufficient to make a decisive statement at this time.

Together, the improvements on the correlation between experimental and calculated R_{1rho} rates while including dynamics as obtained from MD calculations with the Amber ff19SB forcefield, indicates that that forcefield is a reasonable representation of physical reality.

29

4.2 Our work is closely related to reference (18). There, it is demonstrated that one can experimentally detect motion of individual ^{1}H-^{1}H vectors by comparing the intensities of ROESY and NOESY cross peaks (actually in a series of off-resonance ROESYs). In three ways their approach is superior to ours: (1) they detect motion without depending on computation; (2) the information pertains to individual relaxation vectors; (3) no isotope labeling is needed. However, by using cross peaks intensities, one runs into the complication of spin-diffusion. The latter can be circumvented by using very short NOE/OE mixing times, where the NOE/ROE cross peak heights are approximately proportional to the cross-relaxation rates. Regretfully, such short mixing time spectra are not very sensitive, and the approach is limited to very small proteins with very high concentrations (a 10 mM sample of BPTI was used).

Our approach is less elegant but can be applied to samples with lower concentrations (we used 1 mM). Our experiment is not affected by spin-diffusion (i.e., we quantitate what corresponds to the "diagonal" of the ROESY). In order to circumvent our problem with cross-correlated R_2 relaxation, we actually use the most sensitive experiments (short relaxation times) for our analysis. Last, and not least, our experiment, combined with calculation, is sensitive to radial motions (distance variations) whereas theirs is not (because they use the ratio of NOESY and ROESY intensity, which have the same distance dependencies).

4.3 In Figure S8 we compare experimental and calculated ^{1}H-^{15}N rates from a 200 ns MD trajectory. One sees that the correspondence for these rates is excellent (given the experimental uncertainties). The one computed point that lies outside the experimental error range, belongs to Gly38, in a loop. Apparently the current forcefield predicts too much motion for this loop.

4.4 The ^{1}HN-^{15}N dipolar + ^{1}HN CSA relaxation comprise a full 32% of the total ^{1}HN relaxation rates. According to the HydroNMR calculations, these relaxation rates are affected by anisotropic rotational diffusion with a variation of 6% (See also Figure S6). These variations should thus correspond to 1.6% of the total ^{1}HN relaxation rates. One would thus expect that one maybe just detect the effect of these variations in our computations. However, including anisotropic diffusion makes the fit with experiment worse (see Table 1, rows 4,5 and rows 17,18). It is possible that the anisotropic (angular) diffusion of the 1HN-1HX vectors may compensate for the anisotropic effects of the ^{1}HN-N vectors. Taking into account anisotropic diffusion for the thousands of ^{1}HN-^{1}HX vectors is in principle possible by referring to the diffusion tensor as

30

computed from HydroNMR. However, at this stage, we decided that the possible improvement is too small to warrant the effort.

4.5 Why is the rigid fit for R_{1rho} at 283K is so much worse ($R^2=0.22$) than at 303K ($R^2=0.51$)?   The difference cannot be due to the precision of the experiments, which have average uncertainties of 2 and 1% respectively (see Table 1, rows 1 and 8). We offer the following possible explanation. According to the MD simulations, there are fluctuations with a time scale of around 1 ns (e.g., see Figure 4). Motions at that timescale are likely to be statistically independent of the overall motion ($\tau_c=5.96$ ns). They do contribute up to 10% to ^{1}HN NMR relaxation. It may be that neglecting these motions in the rigid calculations at 283K contributes to the low R^2 of 0.2. Including them (as well as overall order parameters) thus makes a dramatic difference ($R^2\sim0.5$)   At 303K, these motions are physically difficult to distinguish from the overall rotational diffusion ($\tau_c=3.6$ ns) and couple and merge with the latter. Not including them in the rigid calculation is then less of a problem ($R^2=0.5$). The improvement by including local motion than results in a smaller change in R^2.

4.6 How can it be that the rigid calculations have the "helical phase" wrong (see Figures 6 and 10) , while the dynamical calculations do approach the experimental "phase"? The rigid "phase" is determined by the number of ^{1}HN-^{1}HX interactions. These are smaller for HN at the solution side of the helix as compared to the inside side of the helix. Including dynamics in the calculations likely breaks this simple pattern.

4.7

What can be improved? While inclusion of dynamics in the R_{1rho} calculations significantly increases the correlation with experimental data, there is clear room for improvement. At first one would suggest including anisotropic rotational diffusion in the calculation. However, including orientation dependent τ_c values for the ^{1}H-^{15}N dipoles (which vary by 10%, see Figure S8) makes correspondence between experiment and calculations worse (see Table 1, row 5).   Because the ^{1}HN-^{1}HX vectors point in many different directions, the effect of orientational anisotropy on the sum of the relaxation rates is averaged out. It has not been included in the computations. While the slope of the correlation for the 303K data with the calculation is reasonable (see Figure 9b), it is badly off for the 283K data (Figure 5). True, only a few points above 30 s^{-1} drive the slope down (L5, I6 and F52, from left to right). These same outliers also occur in the rigid case (Figure

31

3) and thus the forcefield cannot be at fault.   The large experimental rates are not erroneously large because relaxation cross correlation has been neglected. As is shown in (40), fitting single exponentials to a multi-exponential relaxation curve will yield rates that are rather too low than too high. At present we can just offer one explanation: the amides of L5, I6 and F52 are less than 4 Å from each other; possibly they are affected by a common very fast conformational exchange broadening which has not been suppressed by the 10 kHz spinlock.

4.8 Motions slower than the rotational correlation time (ns) will not contribute to the decay of the auto correlation function. However, conformational changes, even if they do not directly contribute to exchange broadening (i.e., $10^5 < k_{AB}$, $k_{BA} < 10^9 s^{-1}$; see equation Equation 1 and discussion thereof), will change distances in the molecule and therefore change the amplitude of the relaxation driving term (see the distance dependence in, e.g., Eq 8). In reality, such exchange processes will result in averaging of different relaxation rates belonging to the different conformations. In case of MD trajectories, one can try to capture those variations by averaging the 5 ns AC function (i.e., the length of the rotational correlation time) over an extended MD run. We used a 200 ns run and should thus be sensitive conformational changes with time scales up to ~100 ns.

4.9 Can the approach be extended to larger proteins? The experiments were carried out for the small protein GB1. The experiments and computational results are of value to the fundamentals of protein science. However, can these experiments and data analysis also be extended to larger proteins which may be of greater biological importance? Provided that 200 μM samples can be made, the sensitivity of the R_{1rho} experiment is likely sufficient, but one still needs a well-resolved ^{15}N-^1H HSQC to analyze the data. The latter limits protein size to about 20 kDa, maybe 30 kDa at very high field. There are, of course, many proteins of biochemical interest that fall under this 20 kDa limit.

If one resorts to perdeuteration of the aliphatics (53) to improve the ^{15}N - HSQC or TROSY, extra complications occur in the interpretation of the data. The perdeuteration needs to be virtually 100% complete, because a few ^1H instead of ^2H here and there will dominate the relaxation of the ^1HN. TROSY also gives yields additional complications as the unknown variability of the ^1HN CSA tensor *orientation* will affect the ^1HN cross-correlated R_2 rate in unknown ways.

It is thus reasonable to project that a 20-30 kDa ^{15}N labeled protein, using an ultra-high field spectrometer can yield sufficiently sensitive with a R1rho-HSQC relaxation data. Of course

32

– a high resolution (crystal) structure needs to be available as well for the analysis of the results in terms of dynamics.

Focusing on Methyl TROSY, the "goto" experiment for very large proteins (54), will not help much either – imperfections in perdeuteration will also be a dominant problem in relaxation and interpretation.

One possibility is to extend the experiment to aromatic protons, using a ^{13}C-^{1}H HSQC as a read-out. Experimentally this is feasible, but complications arise in the interpretation because aromatic protons are difficult to assign, while micro-second ring flips, if present, will average the ^{1}H-environment of the "equivalent" ring protons, complicating analysis.

5   Conclusion.

The dramatic improvement in both the average rate and the R^2 of fit for computed and experimental ^{1}HN R_{1rho} rates for GB1 when incorporating dynamics, cannot *prove* that protein dynamics is pervasive, but strongly points in that direction. Taking the static structure to be either the crystal structure or an average from the simulation yields average relaxation rates that are about 30% higher than experiment (at 283K), whereas including the conformational fluctuations from the simulation cuts this deviation about in half, to 16%. The corresponding overestimates of rates at 303K are 54% for the static structures and 22% when fluctuations are included. The variation of rates among amide protons (as measured by the correlation coefficient) is also much better reproduced by calculations including the effects of conformational fluctuations than from the static structures we have examined. Our NMR experiment and data interpretation / calculation probes coordinate fluctuations between backbone and sidechain spins that are not sensed by other NMR relaxation experiments (except NOESY which is difficult to analyze, especially for larger proteins). As such, this work provides novel insight into the nature of conformational fluctuations that are present in even small globular proteins. The work also suggests that the atomic fluctuations as produced by AMBER, using the ff19SB forcefield, must be a reasonable representation of physical reality. Perhaps one can use this comparison between experimental and computational data to improve future forcefields.

6.Methods and Materials:

6.1 NMR Measurements and data fitting.

The ^{1}HN R_{1rho} – ^{15}N-^{1}H HSQC relaxation experiments on GB1 (see Figure S2) were carried out at 303K on a Bruker 600 MHz instrument at the Canberra NMR Facility, Australia, remotely

33

operated by the author, using a sample of 1 mM ^{15}N-^{13}C labelled GB1 as provided by Dr. G. Otting. The sample temperature was set at 30 ^{0}C. The ^{1}HN were selectively excited with a Q5 Gauss Cascade of 1.33 ms, centered at 8.5 ppm, exciting +/- 1.2 ppm. A spinlock with 14 kHz was applied for 5, 10, 15 and 20 ms. The complete NMR spectral parameters for these experiments are reported in the SI. The same parameters were chosen to record the 283K data at the 600 MHz Bruker instrument at the Magnetic Resonance Research Center in Nijmegen, the Netherlands, using a sample of 20 mg/mL GB1 ^{13}C/^{15}N in H_2O, 20 mM NaPi, pH 7.0., purchased from Cortecnet Europe, 91940 Les Ulis, France. We used a spinlock fields of 6 kHz and 12 kHz, which locking times of 3, 5, 7, 10, 13 and 20 ms. The ^{15}N relaxation experiments (^{15}N R1, ^{15}N-R_2-CPG and ^{1}H-^{15}N NOE) were also collected at the Nijmegen Center, and analyzed with a MODELFREE software package.

The experimental R_{1rho} relaxation data were fitted to a single exponential – double exponentials did not improve the fit. Several examples are shown in the SI. The error of fit was determined using a jack-knife procedure by repeatedly fitting the experimental data in which single data points were omitted at random . The reported error of fit is the RMSD of the fitted relaxation rates. A Table with complete relaxation data is provided in the SI.

6.2 MD calculations

The GB1 molecular dynamics calculations were carried out using the program AMBER 19 with the ff19SB protein forcefield (48). The protein, based on the crystal structure coordinates 2qmt.pdb (resolution 1.1 Å) was embedded in an octahedral box of 5534 water molecules, described with the OPC model (50). Equilibration for 120 ns using a Langevin thermostat and Monte Carlo barostat brought the system to the desired average temperature and a pressure of 1 atm, with a final density of 1.014 gm/cm^3. This was followed by 250 ns of NVE simulation, using a time step of 2 fs and the SHAKE procedure to constrain bond distances to hydrogens. The final 200 ns were used for relaxation analysis, with snapshots saved every 0.005 ns, for a total of 40,000 frames. An MD frame was selected that had the lowest heavy-atom coordinate RMSD as compared to a non-physical average structure, computed by averaging Cartesian coordinates after removal of overall translation and rotation. These frames were dubbed "DYNAMIC AVERAGE" in Table 1.

6.3. Computational auto correlation functions and relaxation rates

We make the assumption that the dipolar autocorrelation function can be factored into an overall isotropic rotational diffusion with rotational correlation time τ_C, as obtained from ^{15}N

relaxation measurements, and a local motional contribution determined from the MD trajectory (51). While the (anisotropic) rotational correlation time can in principle also be determined from extended MD trajectories, we opted to use the experimental time because : MD estimates of protein diffusion tensors are generally not all that accurate yet (55). Furthermore, even "perfect" simulations are carried out at infinite dilution in protein in a pure solvent, which fails to adequately account for the hydrodynamic environment in actual experiments. Accordingly, we separate overall on local motion by superposing the frames of the MD calculations by minimizing the RMSD between the CA positions for residues 10 - 40. For the calculations we took all 40,000 frames of the 200 ns simulations into account.

A simple program was written to select, for each amide proton, all surrounding protons in a sphere of a certain radius to be selected for the calculations. Calculations with different radii were compared (Table 1, rows 7-12), and we decided that 8 Å is a good choice, yielding on average 100 protons in each sphere. The selection was made using a single reference frame and was applied to all frames. Hence some of the tracked protons could move in or out of the "interaction sphere". The inter-proton vector identifications were written to a file readable by the AMBER cpptraj routines (1).

The local autocorrelation functions (AC) were subsequently obtained from the MD run using the AMBER *cpptraj* routines (1) that use an integration to evaluate the correlation function for the spin pair *ij*:

$$AC_{ij}(\tau) = \left\langle \frac{1}{r^3_{HNi-HXj}(t)} \frac{1}{r^3_{HNi-HXj}(t+\tau)} P_2 \cos\left(\vec{\mu}_{HNi-HXj}(t) \cdot \vec{\mu}_{HNi-HXj}(t+\tau) \right) \right\rangle \qquad [13]$$

Where $\vec{\mu}_{HN-HX}(t)$ is the instantaneous unit vector connecting HN and HX. The angular brackets indicate a time average. This AC is not normalized, and its initial value is given by:

$$AC_{ij}(0) = \left\langle \frac{1}{r^3_{HNi-HXj,}(t)} \frac{1}{r^3_{HNi-HXj}(t)} \right\rangle \qquad [14]$$

The calculated $AC_{ij}(\tau)$ show a fast initial decays τ_{Fij} (typical time constant < 10 ps), a slower decay τ_{Sij} (typical time constant ~ 1 ns, amplitude A_S), with a plateau (A_∞). (e.g., see Figure 8).

35

Together with an isotropic overall rotational auto correlation time τ_R , one may model such a $AC_{ij}(\tau)$ as

$$AC_{ij}(\tau) = exp\left(-\tau/\tau_C\right) \times AC_{ij}(0) \times \left[A_{ij}^{\infty} + A_{ij}^{S} exp\left(-\tau/\tau_{Sij}\right) + \left(1 - A_{ij}^{\infty} - A_{ij}^{S}\right) exp\left(-\tau/\tau_{Fij}\right)\right] \qquad [15]$$

In the following, we keep describing spin pair *ij* but drop for legibility all indices (which will later return):

$$AC(\tau) = exp\left(-\tau/\tau_C\right) \times AC(0) \times \left[A_{\infty} + A_S exp\left(-\tau/\tau_S\right) + \left(1 - A_{\infty} - A_S\right) exp\left(-\tau/\tau_F\right)\right] \qquad [16]$$

We can associate the plateau value A_{∞} with an order parameter S^2 $^1HN^{-1}HX$ for the local motion of vector *ij*. The amplitude A_s and correlation time τ_S describe the motions at a 1 ns time scale.

We formally obtain, by integration, from the auto correlation function [12], the spectral density function

$$J_{\omega} = \frac{2}{5}\left(\frac{A_{\infty}\tau_R}{1 + \omega^2\tau_C^2} + \frac{A_S\tau_1}{1 + \omega^2\tau_1^2} + \frac{\left(1 - A_{\infty} - A_S\right)\tau_2}{1 + \omega^2\tau_2^2}\right) \times AC(0) \qquad [17]$$

where

$$1/\tau_1 = 1/\tau_C + 1/\tau_S$$
$$1/\tau_2 = 1/\tau_C + 1/\tau_F \cong 1/\tau_F \qquad [18]$$

since

$$\tau_F < \tau_S << \tau_C \quad . \qquad [19]$$

the amplitude $\left(1 - A_{\infty} - A_S\right)$ and correlation time τ_F describe the motions at a ns-ps time scale which will not make a significant contribution to relaxation. We may write

$$J_{\omega} = \frac{2}{5}\left(\frac{A_{\infty}\tau_R}{1 + \omega^2\tau_C^2} + \frac{A_S\tau_1}{1 + \omega^2\tau_1^2}\right) \times AC(0) \qquad [20]$$

36

So, to evaluate the effect of local motion on ^{1}HN-^{1}HX relaxation rates, we only need to obtain A_∞, A_S, τ_1 from the individual ACs, by non-linear fitting, while τ_C has been experiemntally determined (or obtained from Hydronmr).

These spectral density functions can be directly inserted in the ^{1}H-^{1}H R_{1rho} relaxation rate equations for a like (spin-locked) spin ij, e.g.:

$$R_{1\rho}^{like} = D^2\left\{9J(\omega_{rf}) + 15J(\omega_H) + 6J(2\omega_H)\right\} \times AC(0)$$
$$\cong D^2\left\{9J(0) + 15J(\omega_H) + 6J(2\omega_H)\right\} \times AC(0)$$

[21]

with

$$D^2 = \frac{1}{8}\left(\frac{\mu_0\gamma_H\gamma_H\hbar}{4\pi}\right)^2$$

[22]

Here, $\mu_0, \gamma_H, \hbar$ are the magnetic permeability of vacuum, the proton gyro-magnetic ratio and Planck's constant divided by 2π, respectively.

Or, for unlike ^{1}HN – ^{1}HX pairs we have

$$R_{1\rho}^{unlike} = D^2\left\{5J(\omega_{rf}) + 9J(\omega_H) + 6J(2\omega_H)\right\} \times AC(0)$$
$$\cong D^2\left\{5J(0) + 9J(\omega_H) + 6J(2\omega_H)\right\} \times AC(0)$$

[23]

We will now expand the unlike-spins relaxation equation using the spectral density function model (eq. 20):

$$R_{1\rho}^{unlike} = D^2\left\{\left[\frac{5A_\infty\tau_C}{1} + \frac{5A_S\tau_1}{1}\right] + \left[\frac{9A_\infty\tau_C}{1+\omega_H^2\tau_C^2} + \frac{9A_S\tau_1}{1+\omega_H^2\tau_1^2}\right] + \left[\frac{6A_\infty\tau_C}{1+4\omega_H^2\tau_C^2} + \frac{6A_S\tau_1}{1+4\omega_H^2\tau_1^2}\right]\right\} \times AC(0)$$

[24]

For the following estimation of relative significance of these terms, we label the six terms in square brackets Eq 24 as C_1, C_2, C_3, C_4, C_5 and C_6. We assume that A_∞ and A_s are 0.5, that τ_C=6 ns, τ_1 =1ns. The calculation was made for a 600 MHz proton frequency.

We obtain C_1=1.5x10^{-8} , C_2=2.5x10^{-9} , C_3=5.3x10^{-11}, C_4=3X10^{-10}, C_5=29.8x10^{-12},

C_6=5.2x10^{-11} (s^{-1}).

37

We may thus safely neglect all terms beyond C2 and obtain:

$$R_{1\rho}^{unlike} \cong D^2 \left[5A_\infty \tau_C + 5A_S \tau_1 \right] \times AC(0)$$

[25]

Finally, the total unlike R_{1rho} rate for amide proton i is the sum over all R_{1rho} rates ij

$$R_{1\rho}^{unlike}(i) = \sum_j D^2 \left[5A_{ij}^\infty \tau_C + 5A_{ij}^S \tau_{1ij} \right] \times AC_{ij}(0)$$

[26]

Where we have reintroduced the subscripts as in Eq (15).

Similarly,

$$R_{1\rho}^{like}(i) = \sum_j D^2 \left[9A_{ij}^\infty \tau_C + 9A_{ij}^S \tau_{1ij} \right] \times AC_{ij}(0)$$

[27]

Since equations (26) and (27) are linear, one may also obtain the R_{1rho} rate for amide proton i also from fitting to the *sum* of the autocorrelation functions ij. This improves the time of the computation by a factor of 100. We have implemented the latter in the computer code and checked the results against the sum of the fits.

These calculations were programmed in Fortran-90. The computations were carried out an Apple iMac with a 3.6 GHz Quad-Core Intel Core i7, running MacOS 11.6 (Big Sur).

38

6.4. Statistics of data comparisons

We characterize the quality of fit between experimental values x_i and the calculated values y_i by three criteria:

(1) Relative RMSD (RMSDR) between the experimental values x_i and the calculated values y_i

$$RMSDR = \frac{1}{<y>}\sqrt{\frac{\sum_{i=1}^{N}\left(x_i - y_i\right)^2}{N-1}}$$

[28]

(2) Pearson Correlation coefficient between the experimental values x_i and the calculated values y_i

$$R^2 = \frac{\left(\sum_{i=1}^{N}(x_i - <x>)(y_i - <y>)\right)^2}{\sum_{i=1}^{N}(x_i - <x>)^2 \times \sum_{i=1}^{N}(y_i - <y>)^2}$$

[29]

Note that R^2 is invariant to separate changes in the location or scale of the x and y values.

(3) Slope of the least-squares linear trend line.

$$Slope = \frac{\sum_{i=1}^{N}(x_i - <x>)(y_i - <y>)}{\sum_{i=1}^{N}(x_i - <x>)^2}$$

[30]

(4) "Crystallographic" R factor (46)

$$R = \frac{\sum_{i=1}^{N}\left|x_i - y_i\right|}{\sum_{i=1}^{N}\left|x_i\right|}$$

[31]

39

APPENDIX

Evaluation of scalar coupling-mediated TOCSY coherence transfer from amide to alpha protons using a constant phase spin-lock field.

For this effect, also known as homo-nuclear cross polarization, TOCSY or HOHAHA, we have the following Hamiltonian in the lab frame:

$$H = I_z\left(\omega_I\right) + S_z\left(\omega_S\right) + \pi J I.S$$
$$+ \omega_1 exp\left(-iI_z\omega_{RF}\right) I_x exp\left(+iI_z\omega_{RF}\right)$$
$$+ \omega_1 exp\left(-iS_z\omega_{RF}\right) S_x exp\left(+iS_z\omega_{RF}\right) \tag{32}$$

where

$$\omega_I = frequency\ I\ (radians)$$
$$\omega_S = frequency\ S\ (radians)$$
$$J = scalar\ coupling\ (Hz)$$
$$\omega_{RF} = frequency\ of\ spinlock\ field(radians)$$
$$\omega_1 = amplitude\ of\ spinlock\ field(radians)$$

The Hamiltonian in the rotating frame of the r.f. frequency is written as

$$H = I_z\left(\omega_I - \omega_{RF}\right) + S_z\left(\omega_S - \omega_{RF}\right)$$
$$+ \omega_1 exp\left(-iI_z phi_I\right) I_x exp\left(+iI_z phi_I\right)$$
$$+ \omega_1 exp\left(-iS_z phi_S\right) S_x exp\left(+iS_z phi_S\right)$$
$$+ \pi J exp\left(-iI_z phi_I\right) I_x exp\left(+iI_z phi_I\right) \times exp\left(-iS_z phi_S\right) S_x exp\left(+iS_z phi_S\right)$$
$$+ \pi J exp\left(-iI_z phi_I\right) I_y exp\left(+iI_z phi_I\right) \times exp\left(-iS_z phi_S\right) S_y exp\left(+iS_z phi_S\right)$$
$$+ \pi J I_z S_z \tag{33}$$

where

phi_I is the acquired phase angle between I and r.f . during the integration interval

phi_S is the acquired phase angle between S and r.f . during the integration interval

40

We wrote a numerical integration program for the Liouville-von Neumann equation:

$$\frac{d\sigma(t)}{dt} = -i\left[H(t), \sigma(t)\right]$$

[34]

Using the Hamiltonian in equation [33]. The simulations ran for 0.1 second.

The simulation conditions were:

$$J = 10\ Hz$$

$$\frac{\omega_1}{2\pi} = 10000\ Hz$$

$with$

$$\rho(0) = I_x$$

[35]

When placing the spinlock field carrier between two resonances 1200 Hz apart

$$\frac{\left(\omega_I - \omega_{RF}\right)}{2\pi} = -600\ Hz$$

$$\frac{\left(\omega_S - \omega_{RF}\right)}{2\pi} = +600\ Hz$$

[36]

On obtains, by numerical integration of Eq 34, full transfer I_x to S_x in 0.1 sec , as expected.

41

If one instead sets

$$\frac{\left(\omega_I - \omega_{RF}\right)}{2\pi} = -600 \; Hz$$

$$\frac{\left(\omega_S - \omega_{RF}\right)}{2\pi} = +700 \; Hz \qquad\qquad [37]$$

, one obtains 90 % I_x, and 10% S_x in 0.1 second.

If one instead sets for the actual settings as used at the instrument (amides at 7.5 ppm, alphas at 4.5 ppm, spinlock carrier at 8.5 ppm)

$$\frac{\left(\omega_I - \omega_{RF}\right)}{2\pi} = +600 \; Hz$$

$$\frac{\left(\omega_S - \omega_{RF}\right)}{2\pi} = +2400 \; Hz \qquad\qquad [38]$$

, one obtains 99.9% I_x, and 0.1% S_x

One concludes that there is no significant TOCSY transfer between amides and Ha with a 10 kHz the spinlock field at 8.5 ppm.

7. Acknowledgements

42

REFERENCES

1.   Case, D. A., Cheatham, T. E., 3rd, Darden, T., Gohlke, H., Luo, R., Merz, K. M., Jr., Onufriev, A., Simmerling, C., Wang, B., and Woods, R. J. (2005) The Amber biomolecular simulation programs. *J Comput Chem* **26**, 1668-1688

2.   Hansson, T., Oostenbrink, C., and van Gunsteren, W. (2002) Molecular dynamics simulations. *Curr Opin Struct Biol* **12**, 190-196

3.   Van Der Spoel, D., Lindahl, E., Hess, B., Groenhof, G., Mark, A. E., and Berendsen, H. J. (2005) GROMACS: fast, flexible, and free. *J Comput Chem* **26**, 1701-1718

4.   Brooks, B. R., Brooks, C. L., 3rd, Mackerell, A. D., Jr., Nilsson, L., Petrella, R. J., Roux, B., Won, Y., Archontis, G., Bartels, C., Boresch, S., Caflisch, A., Caves, L., Cui, Q., Dinner, A. R., Feig, M., Fischer, S., Gao, J., Hodoscek, M., Im, W., Kuczera, K., Lazaridis, T., Ma, J., Ovchinnikov, V., Paci, E., Pastor, R. W., Post, C. B., Pu, J. Z., Schaefer, M., Tidor, B., Venable, R. M., Woodcock, H. L., Wu, X., Yang, W., York, D. M., and Karplus, M. (2009) CHARMM: the biomolecular simulation program. *J Comput Chem* **30**, 1545-1614

5.   Bouvignies, G., Meier, S., Grzesiek, S., and Blackledge, M. (2006) Ultrahigh-resolution backbone structure of perdeuterated protein GB1 using residual dipolar couplings from two alignment media. *Angew Chem Int Ed Engl* **45**, 8166-8169

6.   Eisenmesser, E. Z., Millet, O., Labeikovsky, W., Korzhnev, D. M., Wolf-Watz, M., Bosco, D. A., Skalicky, J. J., Kay, L. E., and Kern, D. (2005) Intrinsic dynamics of an enzyme underlies catalysis. *Nature* **438**, 117-121

7.   Kern, D., Eisenmesser, E. Z., and Wolf-Watz, M. (2005) Enzyme dynamics during catalysis measured by NMR spectroscopy. *Methods Enzymol* **394**, 507-524

8.   Brooks, C. L., 3rd, Onuchic, J. N., and Wales, D. J. (2001) Statistical thermodynamics. Taking a walk on a landscape. *Science* **293**, 612-613

9.   Lee, A. L., Kinnear, S. A., and Wand, A. J. (2000) Redistribution and loss of side chain entropy upon formation of a calmodulin-peptide complex. *Nat. Struct. Biol.* **7**, 72-77

10.   Kay, L. E., Torchia, D. A., and Bax, A. (1989) Backbone dynamics of proteins as studied by ^{15}N inverse detected heteronuclear NMR spectroscopy: application to staphylococcal nuclease. *Biochemistry* **28**, 8972-8979

11.   Smith, A. A., Ernst, M., Riniker, S., and Meier, B. H. (2019) Localized and Collective Motions in HET-s(218-289) Fibrils from Combined NMR Relaxation and MD Simulation. *Angewandte Chemie-International Edition* **58**, 9383-9388

12.   Barth, A. (2007) Infrared spectroscopy of proteins. *Biochim Biophys Acta* **1767**, 1073-1101

13.   Mancini, T., Mosetti, R., Marcelli, A., Petrarca, M., Lupi, S., and D'Arco, A. (2022) Terahertz Spectroscopic Analysis in Protein Dynamics: Current Status. *Radiation* **2**, 100-123

14.   Demchenko, A. (1986) Fluorescence analysis of protein dynamics. *Essays Biochem* **22**, 120-157

15.   Choy, W. Y., Shortle, D., and Kay, L. E. (2003) Side chain dynamics in unfolded protein states: an NMR based 2H spin relaxation study of delta131delta. *J Am Chem Soc* **125**, 1748-1758

16.   Bonvin, A. M., Rullmann, J. A., Lamerichs, R. M., Boelens, R., and Kaptein, R. (1993) "Ensemble" iterative relaxation matrix approach: a new NMR refinement protocol applied to the solution structure of crambin. *Proteins* **15**, 385-400

17. Vogeli, B. (2014) The nuclear Overhauser effect from a quantitative perspective. *Progress in Nuclear Magnetic Resonance Spectroscopy* **78**, 1-46

18. Schleucher, J., and Wijmenga, S. S. (2002) How to detect internal motion by homonuclear NMR. *J Am Chem Soc* **124**, 5881-5889

19. Smith, C. A., Mazur, A., Rout, A. K., Becker, S., Lee, D., de Groot, B. L., and Griesinger, C. (2020) Enhancing NMR derived ensembles with kinetics on multiple timescales. *Journal of Biomolecular Nmr* **74**, 27-43

20. Schmidt, H. L., Sperling, L. J., Gao, Y. G., Wylie, B. J., Boettcher, J. M., Wilson, S. R., and Rienstra, C. M. (2007) Crystal polymorphism of protein GB1 examined by solid-state NMR spectroscopy and X-ray diffraction. *J Phys Chem B* **111**, 14362-14369

21. Boulat, B., and Bodenhausen, G. (1993) Measurement of proton relaxation rates in proteins. *J. Biomolecular NMR* **3**, 335-348

22. Vold, R. L., and Vold, R. R. (1978) Nuclear Magnetic-Relaxation in Coupled Spin Systems. *Prog. NMR Spectrosc.* **12**, 79-133

23. Abergel, D., and Palmer, A. G. (2004) Approximate solutions of the Bloch-McConnell equations for two-site chemical exchange. *Chemphyschem* **5**, 787-793

24. Hansen, A. L., Lundstrom, P., Velyvis, A., and Kay, L. E. (2012) Quantifying Millisecond Exchange Dynamics in Proteins by CPMG Relaxation Dispersion NMR Using Side-Chain H-1 Probes. *J Am Chem Soc* **134**, 3178-3189

25. Iwahara, J., Tang, C., and Marius Clore, G. (2007) Practical aspects of 1H transverse paramagnetic relaxation enhancement measurements on macromolecules. *Journal of Magnetic Resonance* **184**, 185-195

26. Toyama, Y., Rangadurai, A. K., and Kay, L. E. (2022) Measurement of H-1(alpha) transverse relaxation rates in proteins: application to solvent PREs. *Journal of Biomolecular Nmr* **76**, 137-152

27. Brüschweiler, R. P. (1991) *Structural dynamics of biomolecular monitored by nuclear magnetic resonance relaxation* Ph.D., ETH Zurich

28. Abragam, A. (1961) *The Principles of Nuclear Magnetism*, Clarenden Press, Oxford

29. Goldman, M. (1988) *Quantum Description of High-Resolution NMR in Liquids*, Clarendon Press, Oxford

30. Segawa, T. F., and Bodenhausen, G. (2013) Determination of transverse relaxation rates in systems with scalar-coupled spins: The role of antiphase coherences. *J Magnetic Resonance* **237**, 139-146

31. Bothner-By, A. A., Stephens, R. L., Lee, J., Warren, C. D., and Jeanloz, R. W. (1984) Structure determination of a tetrasaccharide: transient nuclear Overhauser effects in the rotating frame. *J. Am. Chem. Soc.* **106**, 811-813

32. Davis, D. G., Perlman, M. E., and London, R. E. (1994) DIRECT MEASUREMENTS OF THE DISSOCIATION-RATE CONSTANT FOR INHIBITOR-ENZYME COMPLEXES VIA THE T-1-RHO AND T-2 (CPMG) METHODS. *Journal of Magnetic Resonance Series B* **104**, 266-275

33. Englander, S. W., Downer, N. W., and Teitelbaum, H. (1972) Hydrogen exchange. *Annual review of biochemistry* **41**, 903-924

34. Vendruscolo, M., Paci, E., Dobson, C. M., and Karplus, M. (2003) Rare fluctuations of native proteins sampled by equilibrium hydrogen exchange. *J. Am. Chem. Soc.* **125**, 15686–15687

44

35. Best, R. B., and Vendruscolo, M. (2006) Structural Interpretation of Hydrogen Exchange Protection Factors in Proteins: Characterization of the Native State Fluctuations of CI2. *Structure* **14**, 97-106

36. Schweiger, A., Braunschweiler, L., Fauth, J., and Ernst, R. R. (1985) Coherent and incoherent echo spectroscopy with extended-time excitation. *Phys Rev Lett* **54**, 1241-1244

37. Bax, A. (1989) Homonuclear Hartmann-Hahn experiments. *Methods Enzymol* **176**, 151-168

38. Goldman, M. (1984) Interference effects in the relaxation of a pair of unlike spin 1/2 nuclei. *J. Magn. Reson.* **60**, 437-452

39. Fischer, M. W. F., Majumdar, A., and Zuiderweg, E. R. P. (1998) Protein NMR relaxation: theory, applications and outlook. *Prog. NMR Spectrosc.* **33**, 207-272

40. Zuiderweg, E. R. P. (2022) Multispin Cross-Correlated Transverse Dipolar NMR Relaxation in Solution. *Concepts in magnetic resonance part A* **2022**, 1-10

41. Loth, K., Pelupessy, P., and Bodenhausen, G. (2005) Chemical shift anisotropy tensors of carbonyl, nitrogen, and amide proton nuclei in proteins through cross-correlated relaxation in NMR spectroscopy. *J Am Chem Soc* **127**, 6062-6068

42. de la Torre, J. C., Huertas, M. L., and Carrasco, B. (2000) HYDRONMR: Prediction of NMR Relaxation of Globular Proteins from Atomic-Level Structures and Hydrodynamic Calculations. *J. Magn. Reson.* **147**, 138-146

43. Lipari, G., and Szabo, A. (1982) Analysis of NMR Relaxation Data on Macromolecules Using the Model-Free Approach. *Biophys. J.* **37**, A380-A380

44. Cavanagh, J., Fairbrother, W. J., Palmer III, A. G., and Skelton, N. J. (1996) Protein NMR Spectroscopy, Principles and Practice. Academic Press, London. pp 279

45. Daragan, V. A., and Mayo, K. H. (1997) Motional model analyses of protein and peptide dynamics using ^{13}C and ^{15}N NMR relaxation. *Prog. NMR Spectrosc.* **31**, 63-105

46. Morris AL, MacArthur MW, Hutchinson EG, and JM, T. (1992) Stereochemical quality of protein structure coordinates. *Proteins* **12**, 345-364

47. Frericks Schmidt, H. L., Sperling, L. J., Gao, Y. G., Wylie, B. J., Boettcher, J. M., Wilson, S. R., and Rienstra, C. M. (2007) Crystal Polymorphism of Protein GB1 Examined by Solid-State NMR Spectroscopy and X-ray Diffraction. *J Phys Chem B* **111**, 14362-14369

48. Tian, C., Kasavajhala, K., Belfon, K., Raguette, L., Huang, H., Migues, A., Bickel, J., Wang, Y., Pin- Cay, J., Wu, Q., and Simmerling, C. (2020) ff19SB: Amino-Acid-Specific Protein Backbone Parameters Trained against Quantum Mechanics Energy Surfaces in Solution. *J. Chem. Theory Comput.* **16**, 528-552

49. Williams, C. J., Headd, J. J., Moriarty, N. A.-O., Prisant, M. G., Videau, L. L., Deis, L. N., Verma, V., Keedy, D. A., Hintze, B. J., Chen, V. B., Jain, S., Lewis, S. M., Arendall, W. B., 3rd, Snoeyink, J., Adams, P. D., Lovell, S. C., Richardson, J. S., and Richardson, D. C. (2018) MolProbity: More and better reference data for improved all-atom structure validation.

50. Anandakrishnan, R., Baker, C., Izadi, S., and Onufriev, A. V. (2013) Point charges optimally placed to represent the multipole expansion of charge distributions. . *PloS one* **8**, e67715

51. Lipari, G., and Szabo, A. (1982) Model-Free Approach to the Interpretation of Nuclear Magnetic-Resonance Relaxation in Macromolecules. 1. Theory and Range of Validity. *J. Am. Chem. Soc.* **104**, 4546-4559

52. Brüschweiler, R., and Case, D. A. (1994) Characterization of biomolecular structure and dynamics by NMR cross relaxation. *Progress in NMR Spectrosc.* **26**, 27-58

53. Kay, L. E., and Gardner, K. H. (1997) Solution NMR spectroscopy beyond 25 kDa. *Curr. Opin. Struct. Biol.* **7**, 722-731

54. Tugarinov, V., Kay, L. E., Ibraghimov, I., and Orekhov, V. Y. (2005) High-resolution four-dimensional 1H-13C NOE spectroscopy using methyl-TROSY, sparse data acquisition, and multidimensional decomposition. *J Am Chem Soc* **127**, 2767-2775

55. Wong, V., and Case, D. A. (2008) Evaluating rotational diffusion from protein MD simulations. *J Phys Chem B* **112**, 6013-6024